Hydrogen and Carbon Dioxide Uptake on Scalable and Inexpensive Microporous Carbon Foams

Muhammad Irfan Maulana Kusdhany [a,b], Zhongliang Ma [a,c], Albert Mufundirwa [d], Hai-Wen Li [e,f,g*], Kazunari Sasaki [a,d,e,f], Akari Hayashi [d,e,g], Stephen Matthew Lyth [b,f,g,**]

[a] *Department of Mechanical Engineering, Faculty of Engineering, Kyushu University 744 Motooka, Nishi-ku, Fukuoka 819-0395 Japan*

[b] *Department of Automotive Science, Graduate School of Integrated Frontier Sciences, Kyushu University 744 Motooka, Nishi-ku, Fukuoka 819-0395 Japan*

[c] *College of Materials Science and Engineering, Nanjing Tech University, 30 South Puzhu Road, Nanjing, 211816, PR China*

[d] *Department of Hydrogen Energy Systems, Faculty of Engineering, Kyushu University 744 Motooka, Nishi-ku, Fukuoka 819-0395 Japan*

[e] *International Research Center for Hydrogen Energy, Kyushu University, 744 Motooka, Nishi-ku, Fukuoka 819-0395 Japan*

[f] *International Institute for Carbon-Neutral Energy Research (WPI-I2CNER), Kyushu University, 744 Motooka, Nishi-ku, Fukuoka 819-0395 Japan*

[g] *Platform of Inter/Transdisciplinary Energy Research, Kyushu University, 744 Motooka, Nishi-ku, Fukuoka 819-0395 Japan*

[*] *Present address: Hefei General Machinery Research Institute, 888 Changjiang West Road, Hefei 230031, China*

[**] *Corresponding Author Tel:+81-90-1209-8122. E-mail: lyth@i2cner.kyushu-u.ac.jp*

This is a peer-reviewed, accepted author manuscript of the following article: Kusdhany, M. I. M., Ma, Z., Mufundirwa, A., Li, H. W., Sasaki, K., Hayashi, A., & Lyth, S. M. (2022). Hydrogen and carbon dioxide uptake on scalable and inexpensive microporous carbon foams. Microporous and Mesoporous Materials, 343, [112141]. https://doi.org/10.1016/j.micromeso.2022.112141

Abstract

Hierarchically porous carbon foam (CF) and microporous nitrogen doped carbon foam (NCF) were synthesized at gram scale via the one-step thermal decomposition of metal alkoxides. The total hydrogen uptake of CF reached a maximum of 11.0 wt% at 77 K and 9.5 MPa (or 5.2 wt% excess at 3.9 MPa). This large uptake is attributed to large surface area (3452 m^2/g) and pore volume (2.19 cm^3/g). Even at room temperature, the total hydrogen uptake reached 2.50 wt% (or 0.94 wt% excess). Nitrogen doping resulted in lower hydrogen uptake at higher pressure, due to the lower surface area. Interestingly however, slightly improved hydrogen uptake was obtained in NCF at lower pressure compared to CF, and we attribute this to the narrower pore size. Meanwhile, the CO_2 uptake of CF was 15.2 mmol/g at 273 K and 0.5 MPa. The CO_2 uptake of NCF was slightly lower, but the CO_2/N_2 and CO_2/H_2 selectivity were higher. This was attributed to increased isosteric heat of adsorption between CO_2 and the nitrogen-doped carbon surface. This work shows the potential of bulk-synthesized low-cost metal alkoxide-derived carbon foams to be used in gas storage and separation applications.

Keywords: *Carbon Foam, Hydrogen Storage, Carbon Capture, Physisorption, Microporosity*

Introduction

The biggest problem facing society today is climate change, which has already resulted in rising sea levels, extreme heat waves, and irregular weather patterns [1,2]. This climate crisis is largely driven by human emissions of the greenhouse gas carbon dioxide. Over 40% of CO_2 emissions are the result of fossil fuel combustion for energy production [3], so it is important to curb CO_2 emissions from the energy sector. This can be done either by replacing fossil fuels with a carbon neutral energy carrier such as hydrogen, or by directly capturing CO_2, followed by sequestration or utilization.

Hydrogen has high gravimetric energy density, can be produced using renewable energy, and can be utilized to generate electricity in high efficiency fuel cells without emitting CO_2 [4,5]. However, the volumetric density of uncompressed hydrogen gas is extremely low. As such, to successfully supplant fossil fuels, a suitable storage system for hydrogen must be developed. Currently, this is generally achieved in fuel cell electric vehicles (FCEVs) via high-pressure compression of hydrogen gas at 70 MPa. However, the use of compressed hydrogen has several remaining issues. Firstly, the high pressure necessitates the use of heavy storage tanks made from extremely strong but very expensive carbon fiber composites. Second, the metallic parts of hydrogen storage vessels are susceptible to hydrogen embrittlement [6], resulting in the need for thicker, heavier and costly tanks [7]. In the case of polymer-lined tanks, water can degas from the polymer walls, resulting in lowered fuel cell performance [8]. Finally, high pressure hydrogen gas compression up to 70 MPa requires energy equivalent to 12% of the energy stored in the gas, significantly reducing the round-trip efficiency [9]. Storing hydrogen at lower pressure would contribute significantly to overcoming these problems.

Another method of increasing hydrogen storage capacity is via liquification. However, this is extremely energy intensive, requiring an amount of energy equivalent to 30% of the higher heating value of the hydrogen being liquefied [9]. In addition, liquid hydrogen suffers from substantial boil-off losses due to its exceptionally low boiling point (20 K). For example, a computational study estimated that up to 3.3% of liquid hydrogen is vented when transferring from a stationary storage tank to a trailer, and another 2-10% is lost when transferring from trailer to another tank [10]. Moreover, liquid hydrogen cannot theoretically meet DOE volumetric targets for light vehicles [11].

The third major hydrogen storage solution is to make use of metal hydrides [12–15]. By pressurizing hydrogen in the presence of a suitable metal or alloy at moderate temperature, hydrogen atoms will bind with the metal to form a metal hydride. This allows for safer storage at lower pressure and can result in higher volumetric energy density than compressed or liquified hydrogen. However, desorption of hydrogen from the metal hydride is relatively slow and requires elevated temperatures (e.g., up to 300°C) [16]. In addition, some of the most promising metal hydrides for this application contain critical raw materials, making the scale up of this technology problematic [17].

Finally, physisorption of hydrogen onto materials with large surface area has several advantages over the above methods. Being a “solid-state” storage method, physisorption systems are relatively simple to engineer for vehicular use, and reportedly safer compared to liquid or gaseous hydrogen storage [18]. Physisorption is also a fast and reversible process because the interaction relies on weak van der Waals forces. This makes it more efficient than the use of metal hydrides or compressed hydrogen (e.g. at 70

MPa) [19], and physisorption does not require high temperatures as in the case of metal hydrides.

High hydrogen uptake using physisorption reportedly requires materials with large surface area, a high degree of microporosity (especially with pore diameters in the range of 0.6 to 0.7 nm), and large pore volume [20–22]. Researchers have developed many materials to target these particular textural properties, including zeolites, metal organic frameworks (MOFs), activated carbons, and other nanostructured carbons such as graphene and carbon nanotubes [23–28]. Zeolites have adjustable porosity, controllable surface chemistry, and good stability [29], but generally fail to reach large enough surface areas for high adsorption capacity [28–32]. Meanwhile, MCM-41, a widely studied mesoporous silica, was reported to have a hydrogen uptake of just 1.2 wt% at 1 MPa and 77 K despite being doped with nickel [33]. MOFs have higher surface area than zeolites, as well as controllable porosity, but they are expensive, difficult to scale up, and some have poor stability against moisture [29,34]. They have been reported to have appreciable total hydrogen uptake at 77 K (e.g. > 2 wt% at 0.1 MPa and >11 wt% at 7.8 MPa) [35,36], but at room temperature the benchmark materials can achieve only 1 to 2 wt% total uptake, even at high pressure[37].

Microstructured carbon could provide a low cost and more sustainable alternative to the above materials systems. For example, activated carbon is reported to have good performance at 77 K, with the commercial adsorbent “Maxsorb” achieving excess uptake of 5.7 wt% at 3 MPa [38]. However, such activated carbon materials for physisorption are generally synthesized via an energy intensive two-step carbonization and activation process [25,39–41]. Some carbon materials reported for hydrogen uptake even require

MOFs as templates, further increasing cost, and making scale up less likely [42,43]. To date, very few porous carbon materials have achieved large enough hydrogen uptake capacity to meet the DOE systems target of 5.5 wt% gravimetric capacity (even at 77 K) [44]. This situation limits the applicability of carbon-based hydrogen storage materials for mobile applications such as light duty vehicles. Therefore, it is necessary to develop a scalable carbon material for hydrogen physisorption that uses low cost and abundant precursors, requires few processing steps, and avoids the requirement of sacrificial templates.

A second approach to curbing CO_2 emissions from the energy sector is by direct carbon capture and sequestration (CCS). The importance of this was highlighted in a recent study, which showed that even in the most optimistic scenario, CCS must be implemented at large scale if, e.g., Japan is to achieve its CO_2 emissions reduction targets [45]. CO_2 capture can be performed pre-combustion, in combined cycle power plants, where steam reforming is used to convert fossil fuels to a mixture of compressed H_2 and CO_2 (15 to 60%) [46,47]. Alternatively, CCS can be performed post-combustion of fossil fuels, after separation of CO_2 (up to ~14%) from nitrogen (~77%) and other minor gas phases [48]. Finally, CO_2 can be captured from more pure CO_2 streams originating from industrial processes outside the energy industry (such as cement manufacture) [45].

Carbon capture is currently performed at industrial scale using liquid amine sorbents such as ethanolamine. However, this method has some serious issues which must be addressed. For example, amine sorbents are highly corrosive, resulting in damage to equipment and decreasing the lifetime of components. Additives designed to counter this corrosive nature add cost and increase toxicity [49]. In addition, the interaction between

CO_2 and liquid amines is very strong, and therefore incurs a significant energy cost during desorption. As such, alternative physisorption-based solid CO_2 sorbents are promising. Some examples of physisorption-based solid CO_2 sorbents include porous carbons derived from a variety of precursors including resins [50], biomass [51–53], or MOFs [54]. Meanwhile, MOFs [55,56] and zeolites [57] can also be used as CO_2 sorbents in their own right.

Porous carbon CO_2 sorbents generally require similar textural properties to hydrogen sorbents. High surface area, large pore volume, and the presence of micropores (especially with < 0.7 nm pore diameter), are reported to improve CO_2 uptake [58–60] For effective pre- or post-combustion CO_2 capture, high CO_2/N_2 and/or CO_2/H_2 selectivity is also required. Several experimental and computation studies have claimed that CO_2/N_2 selectivity in carbonaceous materials can be improved via nitrogen-doping [61–63]. However, this effect is reported to be relatively small compared to the effect of pore size distribution [61,64].

One class of porous carbons with the potential to act as both a hydrogen sorbent and a carbon dioxide sorbent are carbon foams. In our group, carbon foams with relatively large surface area and high degree of microporosity are synthesized from various sodium alkoxides [65,66]. These are created via a single-step activation process wherein the sodium alkoxide melts and decomposes into products including carbon, sodium carbonate, and sodium hydroxide, as well as hydrogen gas and carbon dioxide. The gaseous products generate a macroporous foam structure via self-blowing, whilst the sodium compounds generate micropores via self-activation. As such the resulting materials can be classified as hierarchically porous self-activated carbon foams. This method is simple, reproducible,

and scalable [65]. These carbon foam materials have previously been reported to have surface area up to 2500 m^2/g [67], have been used as platinum supports in electrocatalysts [68] and preliminarily investigated for hydrogen adsorption at up to 1 MPa [27,69].

A nitrogen-doped analogue of this carbon foam has also been synthesized previously. In early studies, this was done by reacting sodium with ethanol and ethanolamine, followed by pyrolysis, resulting in a material with around 700 m^2/g surface area [70]. Subsequent studies have then used triethanolamine (TEOA) as a nitrogen source, resulting in improved surface area up to 2500 m^2/g [71–73]. This nitrogen-doped carbon foam has been applied as an electrocatalyst support [71,72] or as a metal-free catalyst in its own right [70,73]. This material is of interest in the current work because nitrogen doping reportedly improves CO_2 adsorption on carbon surfaces [61,64].

In this study, we synthesize similar carbon foams which have been optimized to increase their surface area, via the one-step, template-free pyrolysis of sodium ethoxide. We additionally synthesize the analogous nitrogen-doped carbon foam using triethanolamine as a nitrogen source. The hydrogen uptake is investigated at up to 9.5 MPa at 77 K and 298 K, and the carbon dioxide uptake and selectivity is measured at up to 0.5 MPa at 273 K and 298 K. The effect of porosity and nitrogen doping on the hydrogen and carbon dioxide adsorption capacity and selectivity are clarified. To the best of our knowledge, this is the first study on the performance of alkoxide-derived carbon foams for high pressure hydrogen adsorption and carbon dioxide capture.

Experimental

Synthesis

All chemicals were used as received without further purification. 20 g of sodium ethoxide (Wako, Japan) was measured into an alumina crucible and then heated under nitrogen flow in a box furnace (725°C, 3°C/min, 2 hours holding time). After cooling, the resulting carbon was crushed with a mortar and pestle and dispersed in deionized water. The dispersion was magnetically stirred for 24 hours, then vacuum filtered through a 0.2 μm polytetrafluoroethylene (PTFE) membrane until the filtrate was pH neutral. This washing step was performed to remove sodium carbonate and sodium hydroxide impurities remaining after pyrolysis. Finally, the PTFE membrane was dried at 60°C for 24 hours and the carbon foam was scraped from the membrane. Herein this sample is abbreviated as CF.

For synthesis of nitrogen-doped carbon foam, 18 g of sodium ethoxide was measured into tetrahydrofuran solvent (THF, Wako), under nitrogen flow in a round-bottomed flask. The dispersion was a magnetically stirred for 1 hour, and then 6 g of triethanolamine (TEOA, Sigma Aldrich, Japan) was added, followed by a further 24 hours of magnetic stirring in an inert atmosphere. Sodium ethoxide is a strong base (pKa = 15.5) and is therefore capable of deprotonating the alcohol groups in the TEOA (pKa = 7.74). The equilibrium point of this reaction will depend on the ratio of reactants, and the product is a sodium-ion exchanged analogue of TEOA. The THF solvent was then removed and recovered by rotary evaporation at 60°C and 100 Pa. The resulting powder was pyrolyzed under nitrogen flow in a box furnace under the same conditions as for CF (namely, 725°C, 3°C/min, 2 hours holding time), followed by the same washing, vacuum filtering, and drying protocols. Herein this sample is abbreviated as NCF.

Materials Characterization

Samples were characterized by field emission scanning electron microscopy (FE-SEM, SU-9000, Hitachi, Japan) with acceleration voltages of 25 or 30 kV depending on the sample in combination with Energy Dispersive Spectroscopy (EDS) at 30 kV acceleration voltage for elemental analysis; Raman spectroscopy (Renishaw inVia Raman microscope, $\lambda = 532$ nm) with laser power of 25 mW and spot size of 1.5 μm; and powder X-Ray diffraction (XRD, Rigaku SmartLab). Elemental analysis was performed by EDS, X-ray photoelectron spectroscopy (XPS, Ulvac PHI5000 VersaProbe-II), and CHN analysis (Yanaco CHN Corder MT-5).

Gas Sorption Measurements

Before each gas sorption measurement, the samples were degassed at 300 °C for 3 hours to remove any moisture or other adsorbed molecules from the surface. As a comparison for gas sorption testing, a commercially available activated carbon was used (MSC-30, Maxsorb, Kansai Coke & Chemicals Company Ltd, Japan). This material has been widely used in the scientific literature for many adsorption applications, including for hydrogen storage. This means that the accuracy of the adsorption measurements and characterizations in this study can be verified by comparing the data for MSC-30 with those from other studies. Furthermore, it serves as a realistic benchmark for the state-of-the-art of carbonaceous sorbents in the industry today. To determine the porosity of the materials, N_2 adsorption measurements were conducted up to the nitrogen saturation vapor pressure at 77 K (i.e., ~0.1 MPa) using a Belsorp Mini-II (MicrotracBel, Japan). The resulting isotherms were then analyzed using the Brunauer-Emmett-Teller (BET) equation and de Boer's t-plot method to determine the specific surface area and micropore volume, respectively.

In this study excess, total, and absolute uptake are all discussed in detail, and all three have distinctly different definitions. Excess uptake corresponds to the proportion of adsorbed gas molecules with higher density compared to compressed gas molecules at the same temperature and pressure. This is the value obtained directly by the measurement device used in this study. Meanwhile, total uptake corresponds to the total amount of gas residing within the pore volume of the material, both in the form of adsorbed molecules *and* compressed gas. This is calculated from the excess uptake by adding the amount of compressed gas expected to be found in the total pore volume in the given pressure and temperature conditions. The absolute uptake corresponds to the proportion of molecules in the adsorbed layer. This is defined within a fixed distance from the surface. Inside this boundary, adsorbed molecules have higher density than the compressed gas found outside the boundary. The absolute uptake cannot be directly experimentally determined. In this study it is inferred statistically during isotherm model fitting. More detailed descriptions of these different adsorption values can be found in other studies on the topic [74,75] and can be seen graphically in Figure S1.

Excess H_2 uptake isotherms were recorded using Belsorp HP equipment (MicrotracBel, Japan), at 77 K and 298 K, at pressures up to 9.5 MPa using high purity hydrogen (99.9999%). Total hydrogen uptake was calculated from the excess adsorption by considering the amount of gas stored in the total pore volume using the equation below [25]:

$$w_t = w_{exc} + \frac{100 \times \rho_{H_2} \times V_T}{1 + \rho_{H_2} \times V_T} \quad (1)$$

where w_t is total uptake (wt%), w_{exc} is excess adsorption (wt%), V_T is total pore volume (cm^3/g) and ρ_{H_2} is the density of hydrogen (g/cm^3) at a given temperature and pressure, as obtained from the US National Institute of Standards and Technology (NIST) standard reference database number 69 [76].

To further understand the adsorption process, the adsorption branch of each hydrogen sorption isotherm is then fit to several different equations describing different modes of adsorption. The equations/models being compared are: a modified Langmuir equation corresponding to homogeneous monolayer adsorption, the Unilan (Uniform Energy Distribution with Langmuir Local Isotherm) equation which is an extension of the Langmuir equation without the homogeneity assumption, the Toth equation (a monolayer adsorption equation with an empirical heterogeneity parameter), the Modified Dubinin-Raduskevich (MDR) empirical equation corresponding to micropore filling with a homogeneous energy of adsorption, and a heterogeneous version of it called the Modified Dubinin-Astakhov (MDA) equation. The exact parameterizations and assumptions of these equations can be inspected in Table S1.

However, these equations describe absolute adsorption, and not the measured excess adsorption. The difference can be accounted for by using the following equation:

$$n_{exc} = n_{abs} - \frac{\rho_g v_a}{M} = n_{abs}\left(1 - \frac{\rho_g}{\rho_a}\right) \quad (2)$$

Where n_{exc} is the excess adsorbed amount (mmol/g), n_{abs} is the absolute adsorbed amount (mmol/g), ρ_g is the density of the bulk gas phase (g/cm^3), v_a is the adsorbed phase volume, ρ_a is the adsorbed phase density (g/cm^3), and M is molar mass of the adsorbate (g/mmol). The value of v_a and ρ_a cannot be determined directly from the isotherms, however, and

must be estimated/inferred. In this study, three methods of approximating the adsorbed phase volume which have been used in the literature previously are applied and compared. The first method sets ρ_a as equal to the density of liquid hydrogen, and then calculates v_a accordingly at different loadings [77]. The second method assumes v_a is a constant which needs to be fitted during regression, and then allows the density to vary with loading [78] Finally, it is possible to assume that the adsorbed phase is a condensed equilibrium phase [79]. Subsequently, the adsorbed and bulk phases can be approximated to follow something like the law of rectilinear diameter, which means the average value of ρ_a and ρ_g is a linear function of temperature, i.e., $\rho_a + \rho_g = a - b * T$. The variables a and b can then be added as additional parameters to fit. In this case, both the adsorbed density and volume vary with pressure and loading, respectively.

For each equation, the fitting was done simultaneously to isotherms from both the 77K and 298K measurements. The parameters of each equation are inferred using Bayesian statistics via the probabilistic programming language Stan [80]. The Stan codes for these models are also included via a link in the SI. The performance of each model is then evaluated by comparing the expected log pointwise predictive density (ELPD) from leave one out cross validation (i.e., how much probability each model assigns to the original data without seeing them) as well as from visual checks of the posterior predictive plots.

After fitting, the heat of adsorption for hydrogen on MSC-30 is then estimated based on the Unilan fit using the following equation [81]

$$-\Delta h_{ads} = E_{max} - \frac{(1-x)s}{1-\exp\left(\frac{(1-x)s}{RT}\right)} - \frac{xs}{1-\exp\left(\frac{-xs}{RT}\right)} \quad (3)$$

where E_{max} is the maximum energy of adsorption, $x=n_{abs}/n_{max}$ is the fractional coverage, $s=E_{max}-E_{min}$ is the range of energies of adsorption, and R is the universal gas constant. For CF and NCF, meanwhile, the heat of adsorption is estimated using the following equation obtained by combining MDA and a version of the Van't Hoff equation [82]:

$$-\Delta h_{ads} = \alpha \left(\log \frac{n_{max}}{n_{abs}}\right)^{\frac{1}{m}} - R \cdot \frac{\partial(\log P_0)}{\partial\left(\frac{1}{T}\right)} \quad (4)$$

where α is a fitted parameter often referred to as the enthalpic factor, m is a coefficient which indicates heterogeneity, and P_0 is the pseudo-saturation pressure of H_2 at temperature T. The partial derivative for the second term is 0 in this case because the pseudo-saturation pressure is assumed to be a constant during fitting. Thus, the heat of adsorption is assumed to be constant with respect to T, unlike for Unilan.

Excess CO_2 uptake isotherms were recorded using the same Belsorp HP equipment (MicrotracBel, Japan), at pressures up to 500 kPa. The CO_2 isotherms at two different temperatures (273K and 298K) were fitted to the Langmuir, Unilan, MDA, and MDR models. The parameters of the MDA fit for all samples were then used to estimate the heat of adsorption using the same equation as the one used for hydrogen sorption on CF and NCF. In the case of CO_2, however, P_0 is the actual saturation pressure of CO_2 obtained from a NIST database [76], and the partial derivative in the second term is then numerically approximated.

The high-pressure cutoffs (i.e., 9.5 MPa and 500 kPa) are based on the highest pressure available to measure with the available equipment to gain a more complete understanding of the adsorption behavior of the materials. For real-world applications,

the lowest possible pressure with acceptable hydrogen storage capacity should be used, or atmospheric pressure for post-combustion CO_2 capture, or higher-pressure CO_2 for pre-combustion CO_2 capture.

To determine CO_2/N_2 selectivity, further N_2 uptake measurements were performed using the Belsorp Mini-X (MicrotracBel, Japan) at 273 K and 298 K at up to 100 kPa. To calculate selectivity in a gas mixture, the single component isotherm for each gas in the mixture was fitted using either the Unilan (in the case of CO_2 and H_2) or the Langmuir equation (in the case of N_2). Other equations such as MDA, MDR, and Toth were not used because they are thermodynamically inconsistent at low pressures, which may cause problems when extrapolation is needed during computation [83]. Binary mixture adsorption isotherms for 15% CO_2/85% N_2 and 15% CO_2/85% H_2 mixture gases were then simulated from the fitted single component isotherms using Ideal Adsorbed Solution Theory (IAST) using an algorithm based on the widely used python library PyIAST [84,85]. Aside from IAST selectivity, Henry's law selectivity was also calculated by taking the ratio of Henry's constant obtained from the slope at low pressure of each gas.

In addition, the CO_2 adsorption data at 273 K was used in combination with N_2 adsorption data at 77 K to determine pore size distribution of the samples. This dual gas analysis was done by fitting them simultaneously to two different 2-Dimensional Non-Local Density Functional Theory (2D-NLDFT) kernels [86] using the SAIEUS software from Micromeritics. For additional comparison, classical models fitted to nitrogen sorption data such as the Barrett-Joyner-Halenda (BJH) analysis and the micropore analysis plot (MP plot) were used to look at mesopore and micropore distribution, respectively.

Results and Discussion

Synthesis Yield

The yield of our porous carbon materials is shown in Table 1. For NCF, ~3 grams were lost during mixing of TEOA and sodium ethoxide in THF due to residue on the sides of the flask and evaporation. The yield after pyrolysis is significantly larger than the final yield after washing, due to the removal of water-soluble Na-containing products. NCF has a slightly higher final yield compared to CF, and this is attributed to the addition of triethanolamine (which contains no Na), lowering the sodium to carbon ratio. Calculating the yield based on elemental carbon in the precursors and products weight basis (shown in brackets), the yields of CF and NCF are comparable with high-performance activated hydrochars in the literature [87,88].

Based on these yields and the current bulk price of the precursors (~2 USD/kg), the raw materials cost of producing CF and NCF are estimated to be 47.6 USD/kg and 35.6 USD/kg, respectively. This is about the same as the estimated raw materials costs for MOFs (as of 2017) [89]. However, the processing steps for CF and NCF (i.e. mixing, thermal treatment, purification, etc.) are similar to those for conventional activated carbons, corresponding to an estimated ~1.4 USD/kg (based on a 2008 techno-economic simulation of an activated carbon plant producing 1 million kg of carbon a year) [90]. Meanwhile, a MOF synthesis facility with a scale of 2.5 million kg per year is projected by a 2017 techno-economic analysis to have an average processing cost of ~20 USD/kg[89]. As such the overall cost of CF and NCF production including raw materials and processing is expected to be much lower than for MOFs.

Structural Characterization

SEM images of the different carbon materials are shown in Figure 1. Both samples (CF and NCF) are observed to consist of an open cell structure with micron-scale spheroidal pores separated by thin interconnected graphene-like cell walls. The cell size is ~3 to 5 microns for CF and ~1 to 2 microns for NCF. The difference in cell size is attributed to the difference in viscosity of the precursors upon melting, with the more viscous Na-ion exchanged TEOA resulting in smaller bubbles during foaming. Our previous study on similar materials used atomic force microscopy to confirm that the cell walls are atomically thin [70]. Meanwhile, the MSC-30 reference sample does not have the same type of foam-like structure. CF has the largest particle size of ~300 μm diameter being common (Figure S2a). NCF has the finest particle size (Figure S2b) where even the largest particle is less than 100 μm in diameter. Finally, in MSC-30 there is an even distribution between smaller (<60 μm) particles in combination with larger particles (Figure S2c).

The Raman spectra of the carbon materials (Figure S3a) display three main peaks: the D peak (1350 cm^{-1}); the G peak (1595 cm^{-1}); and the 2D peak (~2660-2710 cm^{-1}). The D peak is attributed to the breathing mode of sp^2 aromatic rings, and only becomes active at the borders between crystallites where translational symmetry is lost. The G peak is due to bond stretching of the rings, whilst the 2D peak is an overtone of the D peak [91,92]. The ratio of the D peak intensity to the G peak intensity (I_D/I_G) can be used as an estimate of disorder (i.e., the relative amount of crystallite boundaries) in a material [92]. CF has an I_D/I_G ratio of 1.00, and NCF has a very slightly higher I_D/I_G ratio (1.01), suggesting that nitrogen doping does not fundamentally change the amount of disorder in the material

in this case. Meanwhile, the value is 0.95 for the MSC-30 reference sample, suggesting that it is slightly less defective compared to CF and NCF.

Two peaks are visible in the powder XRD diffraction patterns (Figure S3b): a large diffraction peak at $2\theta = 22°$ and a smaller peak at $2\theta = 44°$ are attributed to the (002) and (100) planes of turbostratic carbon, respectively [93]. The (002) peaks for CF and NCF have rather large full width at half-maximum (FWHM) of 8.17 and 8.13, respectively, indicating that they are relatively amorphous with a low degree of graphitization compared to MSC-30 (FWHM = 5.37). This is to be expected from the relatively low heat treatment temperature during synthesis (725 °C), whereas graphitization in carbon materials typically occur at much higher temperatures (e. g. ~3000 °C) [94,95].

Chemical Composition

Table 2 shows the atomic concentration of each element in the materials based on XPS data. There is a small amount of sodium detected in CF despite thorough washing. This is attributed to residual sodium-containing byproducts encapsulated inside inaccessible pores in the material, protecting it from dissolution in water. These can only be removed by further heat treatment steps, at the expense of microporosity and cost [72]. In NCF these residues are smaller than the standard error/do not exist because the foaming process does not produce closed cells large enough to trap the Na-containing compounds, as will be explained in the nitrogen adsorption section. The detected nitrogen content of 7.0 at. % in NCF confirms that the nitrogen doping was successful. On the other hand, the trace amounts of nitrogen detected in CF and MSC-30 are well under the standard error for each sample, and no clear signal is observed in the spectrum (Fig. S4). Therefore,

this is attributed to signal noise [96]. The oxygen contents are very similar in both CF and NCF (~6 at. %). Meanwhile, MSC-30 has lower oxygen content. This difference could be attributed to the lower heat treatment temperature for CF and NCF compared to MSC-30. The elemental analysis results obtained using XPS (a quasi-surface sensitive technique), are in agreement with bulk elemental analysis via EDS and CHN analysis (Table S2).

Figure 2 shows the deconvoluted N1s spectra of NCF. Peak fitting shows the presence of pyridinic nitrogen (~398 eV, 27%); graphitic / pyrrolic / hydrogenated pyridinic nitrogen (~400 eV, 55%); protonated nitrogen species (~402 eV, 10%) and oxidized nitrogen (>404 eV, 8%) [97].

Nitrogen Adsorption

The nitrogen adsorption-desorption isotherms of each carbon sample at 77 K are shown in Figure 3a. From these isotherms, we can determine the surface area using the BET equation, as well as the porosity from the isotherm profile, as classified by the International Union of Pure and Applied Chemistry (IUPAC) [98]. CF has the largest surface area of 3452 m^2/g, with an isotherm that is a mixture of Type Ia and Type II adsorption. The steep increase in nitrogen uptake in the lower partial pressure region is attributed to the filling of narrow micropores, followed by mono-multilayer adsorption up to higher partial pressures. A type H4 hysteresis loop is also present, indicating that the adsorption is not completely reversible, as is typical of micro-mesoporous materials [98]. Meanwhile, NCF has a more moderate surface area of 2646 m^2/g (although still large compared to most nitrogen-doped carbons described in the literature)[99,100]. It displays a reversible Type Ia isotherm, indicative of micropore filling in narrow micropores but with an absence of mesopores, unlike CF [98]. MSC-30, meanwhile, has a surface area only slightly lower than CF at 3354 m^2/g, but it instead displays a reversible Type Ib isotherm, commonly found in microporous materials with a broad distribution of micropore sizes, possibly with some proportion of narrow mesopores [98]. The surface area of MSC-30 measured here is in agreement with previously reported values [101]. From the uptake graph at 0.99 relative pressure, we can determine the liquid volume of

adsorbed nitrogen, which corresponds to the total pore volume. The data shows that CF has the largest total pore volume at 2.19 cm^3/g (Table 3), compared with only 1.25 cm^3/g for NCF and 1.82 cm^3/g for MSC-30.

Figure 3b shows the pore size distribution of the samples from NLDFT using simultaneous CO_2/N_2 fitting. It is observed that both CF and NCF have a bimodal pore size distribution in the micropore range. They both have a sharp peak with high intensity at 0.7 nm diameter, revealing the existence of narrow micropores, and a smaller peak at around 1.9 nm. MSC-30, on the other hand, has a smaller and broader peak spanning the micropore range. These results are generally in agreement with the isotherm classifications mentioned in the previous paragraph. Looking at the cumulative pore volume (Figure 3c) in a wider pore size range (up to ~30 nm) further reveals the differences between samples. The cumulative pore volume of CF continues to increase up to the range of larger mesopores, highlighting its hierarchical pore size distribution. Meanwhile, both NCF and MSC-30 are made up almost entirely of micropores, with some small proportion of the pore volume of MSC-30 originating from narrow mesopores. These findings are also generally in agreement with analysis results using more classical methods such as MP and BJH (Figure S6).

If we consider the ratio of the micropore surface area to the total BET surface area (S_{Mic}/S_{BET}) and the ratio of the micropore volume to the total pore volume (V_{Mic}/V_T), it can again be seen that the distribution of pores in CF is hierarchical with micropores comprising a lower ratio of the total, while NCF is almost completely microporous (Table 3). MSC-30, like NCF, is also almost completely microporous by this measure, despite having larger micropores and some narrow mesopores. Another important measure is the

ultramicropore volume V_{UM}, which often dictates the amount of CO_2 able to be adsorbed by a material [64]. Of the materials in this work, NCF has the largest ultramicropore volume, followed by CF and then MSC-30.

One of the key findings here is that the nitrogen doping leads to a narrower pore size distribution in this case. However, it does not seem that the act of doping itself leads to the production of small pores, since the pore distribution of NCF in the micropore range (Figure 3b) looks similar to CF. Rather, we observe that the use of the nitrogen-containing precursor suppresses the production of larger pores. The mechanism behind this observation is not immediately clear, but we speculate that it is related to differences in the viscosity of the precursors during synthesis, which would affect the pore-forming self-blowing process.

It is likely that the reason the materials evaluated here are all microporous is because they are all synthesized by activation with metal hydroxides. In the case of CF and NCF, the materials are "self-activated," with the sodium hydroxide generated during decomposition etching the carbon to form micropores during the single heat treatment step [67]. The synthesis protocols of MSC-30 are not publicly available, but earlier iterations were reportedly made by dehydration of petroleum coke followed by activation using KOH [41].

Hydrogen Uptake

Figure 4 shows the excess and total hydrogen uptake capacity at 77 K, up to 9.5 MPa (see methods for definitions of excess and total uptake). The isotherm profiles

suggest that the adsorption mechanism in this case is either via the filling of micropores or via monolayer adsorption, where most of the adsorption occurs at low pressure regions, followed by a plateau after the micropores are filled/the monolayer is fully occupied. The lack of hysteresis indicates that the adsorption is reversible. The adsorption-desorption process was cycled a total of three times without intermediate heating or pretreatment steps, and the fluctuation in hydrogen uptake is less than ± 5 % (Figure S9). In addition, the BET surface area did not change after the measurements. These points confirm that structure of the carbon itself is not affected by the adsorption / desorption process.

The maximum excess hydrogen adsorption for CF is 5.2 wt%, whilst the total uptake is 11.0 wt% at 9.5 MPa. This significantly exceeds the ultimate US Department of Energy (DOE) targets for onboard hydrogen storage in light-duty vehicles [44], although we note that this 5.5 wt% target is for the entire storage system including tanks and cryo-insulation. The high values are attributed to the large surface area and high pore volume. Meanwhile, NCF has a maximum excess hydrogen adsorption of 5.0 wt%, and a total uptake of 7.9 wt% at 9.5 MPa. The slightly lower excess uptake is attributed to its smaller surface area, while the much smaller total uptake is due to its smaller pore volume, allowing the pores to accommodate less bulk gas. The maximum excess hydrogen uptake of MSC-30 is 5.6 wt%, which is slightly higher than that of CF, *despite* the slightly lower surface area. This is perhaps due to the higher micropore volume ratio (V_{Mic}/V_T in Table 3) in MSC-30 leading to improved interactions with hydrogen. The total uptake for MSC-30 is 10.1 wt% at 9.5 MPa, which is slightly lower than that of CF. This difference is attributed to two factors: i) the smaller pore volume in MSC-30 leading to less gaseous

hydrogen storage in the voids; and ii) the faster decrease in excess adsorption of MSC-30 after reaching its maximum, compared to the more gradual slope in CF.

This decrease in excess adsorption value after reaching a maximum is an interesting behavior caused by saturation. To put it simply, the definition of excess adsorption is the difference between the amount of "high density" hydrogen (i.e., hydrogen adsorbed on the surface) and the amount of "low density" hydrogen (i.e., gaseous hydrogen). After the hydrogen adsorption saturates, the pressure continues to rise, leading to an increase in the density of gaseous hydrogen, which in turn lowers the apparent excess adsorption value. As such, at 9.5 MPa the excess adsorption capacity of MSC-30 and CF are approximately the same because MSC-30 saturates at a lower pressure than CF. The later saturation in CF can be explained by it having larger mesopores and macropores, which contributes more significantly to adsorption at higher pressures [102,103], whereas MSC-30 only has micropores.

To further probe the importance of pore size distribution, the excess hydrogen uptake data was normalized to the surface area (

Figure 4c). In this case, NCF has the best normalized adsorption owing to the lack of mesopores and macropores, which do not contribute as much to hydrogen adsorption capacity. CF has the lowest normalized adsorption because it has a hierarchical pore distribution with many mesopores and macropores. MSC-30 is somewhere in between because it is not hierarchical like CF but consists of larger micropores than NCF. If only the micropore surface area is considered, as in

Figure 4d, the difference in uptake between MSC-30 and NCF virtually vanishes. This shows that micropore surface area is a more important factor to adsorption in those samples than total surface area.

However, even in

Figure 4d CF still has lower normalized uptake at pressures below 7 MPa. CF is very similar in terms of pore size distribution to NCF other than for the existence of wide mesopores (the nitrogen doping does not play a role here).[103] This indicates that the wider mesopores in CF (20-30 nm size) somehow lead to lower adsorption per unit micropore surface area, seemingly in contrast to findings from a previous study [43]. However, although in that work it was observed that hierarchically porous carbons enables higher adsorption than exclusively ultramicroporous sorbents, dividing the uptake of the materials studied in that work at 1 atm by their respective micropore volumes, a similar trend is observed: the hierarchically porous materials accommodate fewer hydrogen molecules per available micropore volume.

Table 4 shows a comparison between the hydrogen uptake of the carbon materials evaluated in this study and other porous materials reported in literature at 77 K and 0.1 MPa (as well as at selected higher pressures reported in the respective studies). At low pressures (up to 0.1 MPa), the excess adsorption on NCF outperforms almost every other material listed, despite its moderate surface area. This might suggest that in low pressure regions, where most adsorbents have not yet saturated, the most dominant factor is pore size distribution rather than surface area. In particular, having narrow pores (<1 nm) where the hydrogen molecule can experience potential fields from both sides of the pore may allow for better binding in NCF [104]. Although NCF is nitrogen doped, several

previous empirical and experimental studies have shown that nitrogen atoms doped into the carbon matrix do *not* significantly affect the binding energy between the surface and the hydrogen molecules, and thus do not play a role here [103,105,106].

With its uptake of 11.0 wt%, CF outperforms e.g., porous aromatic framework PAF-1 by over 20%, and even a high-porosity MOF (i.e., IRMOF-20) by more than 10%. This comparison confirms that the CF material developed in this work outperforms many different porous materials including zeolites, MOFs, and polymer composites in terms of total uptake. We also can see that surface area is not the only determining factor at high pressures, with some MOFs underperforming compared to slightly lower surface area activated carbon materials. Importantly, our material is generated from a low-cost precursor (sodium ethoxide) and is generated in a single thermal treatment step, providing a further advantage compared to other materials published in the literature. However, CF still does not reach the surface area or oxygen content (which is also reportedly important [25,87,103]) of some other porous carbons in literature, such as SF-600 [25], leading to lower performance. Further optimization of synthesis methods to target those properties is planned.

The room temperature storage capacity of each material was also measured (Figure 5). At room temperature, micropore filling is not clearly observed in contrast with the case at 77K. This is attributed to the fact that the adsorbate coverage in this case is much lower and that the interaction between hydrogen and the carbon surface is weak enough that Henry's law can be applied, i.e., the adsorbed phase is similar to a two-dimensional ideal gas so the amount of hydrogen adsorbed varies linearly with pressure [107]. In terms of excess adsorption, the surface area does not appear to play a large role

in determining room temperature adsorption. CF shows very similar performance to NCF despite its much larger surface area, both with a maximum excess adsorption of ~0.95 wt% at 9.5 MPa. MSC30 is outperformed by the other samples with a maximum excess uptake of only 0.72 wt% at 9.5 MPa. The results for MSC-30 are consistent with those reported in the literature (excess uptake of 0.79 wt% at 10 MPa and 298K, as well as 0.67 wt% at 10 MPa and 303K), confirming the calibration of our volumetric measurement device [38,108].

These findings corroborate a previous study on hydrogen physisorption (albeit performed on MOFs) which shows that at 298 K, surface area is not a strong predictor of hydrogen uptake, and micropores larger than 1 nm are no longer effective for hydrogen adsorption [109]. From Figure S10, which is a magnified version of Figure 3c, we see that CF and NCF have similarly large cumulative pore volume under 1 nm, allowing them both to achieve good excess uptake. On the other hand, MSC-30 mostly only has micropores between 1-2 nm and is thus rendered less effective at room temperature. The differences caused by pore size distribution can also be observed clearly in Figure 5c showing the surface area-normalized uptake: NCF has the highest normalized uptake followed by CF and MSC-30, respectively. However, considering the total uptake (i.e., the hydrogen gas stored within the pore volume), CF still has the highest total storage capacity of 2.50 wt% while NCF has a relatively low total uptake of 1.87 wt%. As such, there is a clear tradeoff here between pore volume and pore size distribution. Optimally, the best sorbent for room temperature hydrogen uptake would thus have narrow micropores while maintaining almost atomically thin walls to maximize the pore volume.

The adsorption isotherms (Figure 5) all show a small degree of hysteresis during desorption, which is more prominent at 298K due to the lower absolute adsorption values measured. This could be attributed to the system not reaching equilibrium (i.e., if the desorption step is slower than expected), or a systematic error within the measurement equipment (more likely since the magnitude of this hysteresis is similar for all samples).

The performance of these carbon materials at 298 K was also compared to those reported in literature (Table 5). NCF has the best excess adsorption of all the materials listed at ~10 MPa, beating even the excess adsorption capacity of an advanced MOF (NU-1501-Al) by 20%. Looking at the total uptake, however, CF and NCF are still outperformed by NU-1501-Al due its very large pore volume of ~3 cm^3/g [110]. Nonetheless, the total uptake of our materials is competitive with state-of-the-art synthetic materials in literature while being much cheaper and easier to synthesize.

As explained in the methods section, fitting was also conducted to hydrogen adsorption isotherms to better understand the adsorption mechanism. The best performing model fits for each sample, their associated absolute uptake isotherms, as well as plots of the estimated adsorbed phase densities and volumes can be inspected in more detail in Figures S11-S18. Comparing the quality of the fits based on the differences in ELPD values (Table S3), hydrogen adsorption on CF can be described by either Unilan, MDA, or MDR with similar out-of-sample predictive performance as measured by ELPD. Judging from the posterior plots (Figures S12-S13), the 95% credible interval of MDR seems to give a better fit to the data compared to Unilan at 298K while being a simpler model (i.e., it has fewer fitting parameters), lending more credence to micropore filling being the adsorption mechanism. However, the evidence is not particularly strong. For

NCF, the results are again inconclusive, with both MDA and Unilan being able to explain the isotherms equally well in terms of ELPD. Evaluation of the posterior predictive plots (Figures S14-S15), suggests that the 95% credible interval of the Unilan equation does not line up with the data as well as that of the MDA equation at 298K, again making it more likely that the adsorption happened by micropore filling in the narrow micropores. In the case of MSC-30, there is a tie between the Unilan and Toth adsorption model, meaning that we can be confident that the adsorption mechanism is similar to monolayer adsorption with varying energies, but the distribution of the adsorption energies cannot be discerned from the data in this study alone. Although, comparing the credible intervals to the data for each fit (Figures S17-S18), Unilan is more consistent with the data, indicating a more uniform distribution of adsorption energies.

Another interesting finding from the model fitting has to do with the density of adsorbed hydrogen. When either the adsorbed phase volume or density is set as a fitting parameter, the fit quality improves significantly but the probability distribution of the adsorbed phase density at higher pressures tends towards values that are larger than solid hydrogen density of 0.086 g/cm^3. This is in spite of the fact that the prior probability distribution assigns 99% of the probability to density values that are smaller than liquid hydrogen density (0.0708 g/cm^3). Thus, the data shows a strong preference towards these solid-like adsorbed phase density values. This can either be a result of actual solid-like phases existing in supercritical hydrogen adsorption, as has been suggested by other experimental studies [111,112], or it may also be an effect of model misspecification (i.e., the equations used may be inadequate to describe supercritical sorption, so the fitting parameters tend towards unphysical values to compensate). Either way, further

investigation beyond the scope of this study is needed to answer whether the adsorbed hydrogen is indeed solid-like or if our current models for understanding subcritical sorption no longer works well in the case of supercritical sorption.

It is also possible to infer the heat of adsorption at different uptake values and temperatures from the fitted parameters (Figure 6). The heat of adsorption is derived from the isotherm model with the best fit to the measured data, as described in detail in the methods section. These models are MDA for the cases of CF and NCF, and Unilan for the case of MSC-30, which is why the heat of adsorption in Figure 6 shows a temperature dependency only for MSC-30. CF and NCF have similar heats of adsorption, and these are lower than the case of MSC-30, for which the value is closest to the ideal value for hydrogen storage of 15 kJ/mol [113]. The measured heat of adsorption for MSC-30 is consistent with other results from the literature [111], indicating a good model fit and accurate measurement. However, there is not a strong correlation between heat of adsorption and the maximum excess uptake at 77 K. This is attributed to the fact that the heat of adsorption dictates the shape of the isotherm and how rapidly the maximum uptake is achieved, but ultimately the maximum adsorbed amount is primarily determined by surface area and porosity.

At 298 K, the trend is different - CF and NCF have similar heats of adsorption which are higher than for MSC-30, up to the measured loading of 1 wt%. This trend is similar to that observed when comparing excess adsorbed amounts between the samples at 298K. This indicates that at 298K, the adsorbed amount is strongly affected by the heat of adsorption, which is likely to have a stronger correlation with pore size distribution rather than surface area, dictating the maximum adsorbed amount instead.

CO_2 Capture and Separation

The CO_2 adsorption-desorption isotherms of the different materials were measured at 273 K and 298 K, and the results are shown in Figure 7. First, we discuss the results at a relatively low pressure of 0.1 MPa, which is relevant for post-combustion CO_2 capture. At 0.1 MPa and 273 K, CF and NCF show relatively high CO_2 uptake capacities of 5.65 and 5.79 mmol/g, respectively (corresponding to 24.9 and 25.5 wt%). This is significantly higher than the capacity of MSC-30 (4.57 mmol/g, or 20.1 wt%). Increasing the temperature to 298 K leads to a decrease in capacity (as expected), but both CF and NCF still show a moderate capacity of 3.37 and 3.26 mmol/g, respectively. These values at 298 K are higher than for MSC-30 (2.49 mmol/g) and a solidified amine sorbent reported in literature (3.02 mmol/g) under the same conditions [114].

Meanwhile at a higher pressure of 0.5 MPa (which is more relevant for pre-combustion CO_2 capture), at 273 K CF is the best sorbent with 15.23 mmol/g (67.0 wt%) capacity, closely followed by MSC-30 (15.08 mmol/g, or 66.4 wt%) and then NCF (14.23 mmol/g, or 62.6 wt%). This poor performance of NCF at high pressure may be due to the much smaller pore volume, leading to faster saturation. At 298K, CF still has the highest capacity (9.88 mmol/g, or 43.5 wt%) attributed to its significantly larger pore volume and surface area. This is followed by NCF (9.51 mmol/g), and finally MSC-30 (9.25 mmol/g).

To understand the adsorption mechanism, the isotherms are again fitted with different kinds of adsorption equations. It was found from the ELPD values (Table S4) that the adsorption on all samples is best described by the MDA equation (Figure S19), indicating that the adsorption mechanism is likely to have been micropore filling with

heterogeneous energies of adsorption. To further investigate the interaction between CO_2 and the surfaces of the different samples, the heat of adsorption was calculated using the parameters of the MDA equation at two different temperatures (Figure 8), although the differences between the temperatures are small. Figure 8 shows that CF has a moderate adsorption enthalpy of 20 to 27 kJ/mol, NCF shows the highest value of 22 to 30 kJ/mol, while MSC-30 shows the lowest enthalpy at 19 to 23 kJ/mol. The generally low adsorption enthalpy of these samples indicate that the CO_2 uptake can be attributed to physisorption, in agreement with the highly reversible desorption isotherms in Figure 7. The effect of heat of adsorption is reflected in the surface area-normalized adsorption graph (Figure 7b), clearly showing that NCF has the best normalized capacity, followed by CF and MSC-30.

The improved heat of adsorption on NCF is attributed to a combination of (i) a better pore size distribution, and (ii) the increased basicity of pyridinic and graphitic nitrogen atoms. Pyridinic nitrogen atoms have a lone electron pair while graphitic nitrogen has increased electron density in the delocalized π-orbitals, making them both good electron donors [61]. This should allow them to interact more strongly with CO_2 molecules, acting as a Lewis base. Meanwhile, simulations by Kumar et al. showed that narrow micropores (~0.8 nm diameter) might play a larger role in affecting the isosteric heat of adsorption compared to nitrogen doping [61]. This was also corroborated by a machine learning study which shows that ultramicropore volume has larger relative importance compared to nitrogen content in determining the CO_2 uptake capacity of carbonaceous materials [64].

The importance of pore size distribution may also provide a simple explanation for why CF has a higher enthalpy of adsorption than MSC-30 despite it not being doped with nitrogen - it has ultramicropores while MSC-30 does not. However, although CF has an almost identical ultramicropore volume to NCF, CF has a lower heat of adsorption. This may be caused by only the nitrogen doping, but we speculate that the abundance of mesopores which do not interact strongly with the CO_2 molecules in CF may contribute to this lowered heat of adsorption.

To evaluate the feasibility of using these materials in real-world CO_2 capture applications, the adsorption selectivity of CO_2 over other gases is calculated using either IAST-simulated isotherms or Henry's law, as shown in Table 6. More detailed results regarding selectivity, including the nitrogen adsorption isotherm at 273K and 298K, as well as IAST simulation results across different pressures, can be found in Figures S20-S23. Compared to MSC-30, both CF and NCF have better CO_2/N_2 and CO_2/H_2 selectivity, indicating that they may be better for CO_2 capture and separation in the context of both pre- and post-combustion capture.

However, our carbon foam materials still underperform compared to some state-of-the-art materials recently published in the literature, especially in terms of CO_2/N_2 selectivity (Table 7). This is partly to be expected because our materials have a large proportion of nitrogen-accessible pores, as apparent from the BET measurements. We believe that the improvement in selectivity and uptake in NCF could have been even larger compared to CF considering nitrogen doping and smaller pores. However, this effect is cancelled out by (i) the lower surface area and pore volume, and (ii) the lack of mesopores. This second point comes from an experimental observation which showed

that mesopores disrupt N_2 adsorption significantly more at 298K compared to CO_2 adsorption [115]. Thus, although mesopores are non-conducive to CO_2 adsorption, they could be important in increasing selectivity. This hypothesis has also been supported statistically via a recent deep learning model used to fit large amounts of experimental data [116].

To improve selectivity without sacrificing total uptake capacity in future studies we should consider optimization of the synthesis process to maximize the presence of ultramicropores without losing overall surface area or pore volume. Although increasing the proportion of mesopores might also be a possible strategy to improve selectivity, it does come with negative impacts regarding the uptake capacity, which is not desirable.

Conclusions

To summarize, we have reported a facile method to synthesize hierarchically porous carbon foam (CF) and its nitrogen-doped counterpart (NCF). Both materials have very large BET surface area of 3452 m^2/g and 2646 m^2/g, respectively. A total hydrogen capacity of 11.0 wt% was measured for CF at 77 K and 9.5 MPa, exceeding the ultimate DOE systems target for light-duty vehicle applications (although not accounting for the mass of the tank or cryo-insulation). Even at room temperature, CF displays a total hydrogen uptake of 2.5 wt%, which is comparable to other state-of-the-art sorbents in the literature. NCF has lower hydrogen uptake due to it having lower overall surface area and pore volume. The CO_2 adsorption capacity was also investigated, with CF again outperforming NCF at high pressure due to the influence of pore volume. However, in this case, nitrogen doping resulted in slightly higher selectivity as well as higher isosteric heat of adsorption. This study demonstrates the feasibility of using self-activated porous

carbons in hydrogen storage applications, although further optimization of pore structure is necessary for applications related to CO_2 capture.

Acknowledgements

This work was partially supported by JSPS KAKENHI Grant Number 19H02558; by the Australian Government through the Australian Research Council; and by the Daiwa Anglo-Japan Foundation in the United Kingdom.

Conflicts of Interest

There are no conflicts to declare.

References

[1] B. Marzeion, J.G. Cogley, K. Richter, D. Parkes, Attribution of global glacier mass loss to anthropogenic and natural causes., Science. 345 (2014) 919–921. https://doi.org/10.1126/science.1254702.

[2] E.M. Fischer, R. Knutti, Anthropogenic contribution to global occurrence of heavy-precipitation and high-temperature extremes, Nature Climate Change. 5 (2015) 560–564. https://doi.org/10.1038/nclimate2617.

[3] V. Foster, D. Bedrosyan, Understanding CO2 Emissions from the Global Energy Sector, Live Wire Knowledge Note Series. 5 (2014) 1–12.

http://documents.worldbank.org/curated/en/873091468155720710/Understanding-CO2-emissions-from-the-global-energy-sector (accessed April 22, 2020).

[4] K.T. Møller, T.R. Jensen, E. Akiba, H. Li, Hydrogen - A sustainable energy carrier, Progress in Natural Science: Materials International. 27 (2017) 34–40. https://doi.org/10.1016/j.pnsc.2016.12.014.

[5] S.E. Hosseini, M.A. Wahid, Hydrogen from solar energy, a clean energy carrier from a sustainable source of energy, International Journal of Energy Research. 44 (2020) 4110–4131. https://doi.org/10.1002/er.4930.

[6] S. Lynch, Hydrogen embrittlement phenomena and mechanisms, Corrosion Reviews. (2012). https://doi.org/10.1515/corrrev-2012-0502.

[7] H.-W. Li, K. Onoue, Compressed Hydrogen: High-Pressure Hydrogen Tanks, (2016) 273–278. https://doi.org/10.1007/978-4-431-56042-5_19.

[8] H. Barthelemy, M. Weber, F. Barbier, Hydrogen storage: Recent improvements and industrial perspectives, International Journal of Hydrogen Energy. 42 (2017) 7254–7262. https://doi.org/10.1016/j.ijhydene.2016.03.178.

[9] F. Barbir, Fuel Cell Applications, in: PEM Fuel Cells, Elsevier, 2013: pp. 373–434. https://doi.org/10.1016/b978-0-12-387710-9.00010-2.

[10] G. Petitpas, Boil-off losses along LH2 pathway, US Deparment of Energy, Livermore CA, 2018. https://doi.org/https://doi.org/10.2172/1466121.

[11] P. Bénard, R. Chahine, Storage of hydrogen by physisorption on carbon and nanostructured materials, Scripta Materialia. 56 (2007) 803–808. https://doi.org/10.1016/j.scriptamat.2007.01.008.

[12] A. Rahnama, G. Zepon, S. Sridhar, Machine learning based prediction of metal hydrides for hydrogen storage, part I: Prediction of hydrogen weight percent, International Journal of Hydrogen Energy. 44 (2019) 7337–7344. https://doi.org/10.1016/j.ijhydene.2019.01.261.

[13] L. Pickering, M. V. Lototskyy, M.W. Davids, C. Sita, V. Linkov, Induction melted AB2-type metal hydrides for hydrogen storage and compression applications, Materials Today: Proceedings. 5 (2018) 10470–10478. https://doi.org/10.1016/J.MATPR.2017.12.378.

[14] B.W.J. Chen, M. Mavrikakis, Effects of composition and morphology on the hydrogen storage properties of transition metal hydrides: Insights from PtPd nanoclusters, Nano Energy. 63 (2019) 103858. https://doi.org/10.1016/J.NANOEN.2019.103858.

[15] M. Gambini, T. Stilo, M. Vellini, Hydrogen storage systems for fuel cells: Comparison between high and low-temperature metal hydrides, International Journal of Hydrogen Energy. 44 (2019) 15118–15134. https://doi.org/10.1016/J.IJHYDENE.2019.04.083.

[16] B. Sakintuna, F. Lamari-Darkrim, M. Hirscher, Metal hydride materials for solid hydrogen storage: A review, International Journal of Hydrogen Energy. 32 (2007) 1121–1140. https://doi.org/10.1016/j.ijhydene.2006.11.022.

[17] M. David, S.M. Lyth, R. Lindner, G.F. Harrington, Future-Proofing Fuel Cells, Springer International Publishing, Cham, 2021. https://doi.org/10.1007/978-3-030-76806-5.

[18] R. Strobel, J. Garche, P.T. Moseley, L. Jorissen, G. Wolf, Hydrogen storage by carbon materials, Journal of Power Sources. 157 (2006) 781–801. https://doi.org/10.1016/j.jpowsour.2006.03.047.

[19] M. Moussa, N. Bader, N. Querejeta, I. Durán, C. Pevida, A. Ouederni, Toward sustainable hydrogen storage and carbon dioxide capture in post-combustion conditions, Journal of Environmental Chemical Engineering. 5 (2017) 1628–1637. https://doi.org/10.1016/j.jece.2017.03.003.

[20] Y. Gogotsi, C. Portet, S. Osswald, J.M. Simmons, T. Yildirim, G. Laudisio, J.E. Fischer, Importance of pore size in high-pressure hydrogen storage by porous carbons, International Journal of Hydrogen Energy. 34 (2009) 6314–6319. https://doi.org/10.1016/j.ijhydene.2009.05.073.

[21] M. Armandi, B. Bonelli, C.O. Areán, E. Garrone, Role of microporosity in hydrogen adsorption on templated nanoporous carbons, Microporous and Mesoporous Materials. 112 (2008) 411–418. https://doi.org/10.1016/j.micromeso.2007.10.017.

[22] B. Panella, M. Hirscher, S. Roth, Hydrogen adsorption in different carbon nanostructures, Carbon N Y. 43 (2005) 2209–2214. https://doi.org/10.1016/j.carbon.2005.03.037.

[23] J. Juan-Juan, J.P. Marco-Lozar, F. Suárez-García, D. Cazorla-Amorós, A. Linares-Solano, A comparison of hydrogen storage in activated carbons and a metal-organic framework (MOF-5), Carbon N Y. 48 (2010) 2906–2909. https://doi.org/10.1016/j.carbon.2010.04.025.

[24] A. Ariharan, B. Viswanathan, V. Nandhakumar, Nitrogen-incorporated carbon nanotube derived from polystyrene and polypyrrole as hydrogen storage material, International Journal of Hydrogen Energy. 43 (2018) 5077–5088. https://doi.org/10.1016/j.ijhydene.2018.01.110.

[25] T.S. Blankenship, R. Mokaya, Cigarette butt-derived carbons have ultra-high surface area and unprecedented hydrogen storage capacity, Energy and Environmental Science. 10 (2017) 2552–2562. https://doi.org/10.1039/c7ee02616a.

[26] C.X. Guo, Y. Wang, C.M. Li, Hierarchical graphene-based material for over 4.0 wt % physisorption hydrogen storage capacity, ACS Sustainable Chemistry and Engineering. 1 (2013) 14–18. https://doi.org/10.1021/sc3000306.

[27] S.M. Lyth, H. Shao, J. Liu, K. Sasaki, E. Akiba, Hydrogen adsorption on graphene foam synthesized by combustion of sodium ethoxide, International Journal of Hydrogen Energy. 39 (2014) 376–380. https://doi.org/10.1016/j.ijhydene.2013.10.044.

[28] E. Dündar-Tekkaya, Y. Yürüm, Mesoporous MCM-41 material for hydrogen storage: A short review, International Journal of Hydrogen Energy. 41 (2016) 9789–9795. https://doi.org/10.1016/j.ijhydene.2016.03.050.

[29] P.L. Llewellyn, Storage of hydrogen on nanoporous adsorbents, in: Green Energy and Technology, Springer Verlag, 2019: pp. 255–286. https://doi.org/10.1007/978-981-13-3504-4_10.

[30] H.W. Langmi, D. Book, A. Walton, S.R. Johnson, M.M. Al-Mamouri, J.D. Speight, P.P. Edwards, I.R. Harris, P.A. Anderson, Hydrogen storage in ion-exchanged zeolites, Journal of Alloys and Compounds. 404–406 (2005) 637–642. https://doi.org/10.1016/j.jallcom.2004.12.193.

[31] P. Roy, N. Das, Ultrasonic assisted synthesis of Bikitaite zeolite: A potential material for hydrogen storage application, Ultrasonics Sonochemistry. 36 (2017) 466–473. https://doi.org/10.1016/j.ultsonch.2016.12.032.

[32] J. Dong, X. Wang, H. Xu, Q. Zhao, J. Li, Hydrogen storage in several microporous zeolites, International Journal of Hydrogen Energy. 32 (2007) 4998–5004. https://doi.org/10.1016/j.ijhydene.2007.08.009.

[33] P. Carraro, V. Elías, A.A.G. Blanco, K. Sapag, G. Eimer, M. Oliva, Study of hydrogen adsorption properties on MCM-41 mesoporous materials modified with nickel, International Journal of Hydrogen Energy. 39 (2014) 8749–8753. https://doi.org/10.1016/j.ijhydene.2013.12.038.

[34] K.K. Gangu, S. Maddila, S.B. Mukkamala, S.B. Jonnalagadda, Characteristics of MOF, MWCNT and graphene containing materials for hydrogen storage: A review, Journal of Energy Chemistry. 30 (2019) 132–144. https://doi.org/10.1016/j.jechem.2018.04.012.

[35] D. Sun, S. Ma, Y. Ke, D.J. Collins, H.C. Zhou, An interweaving MOF with high hydrogen uptake, J Am Chem Soc. 128 (2006) 3896–3897. https://doi.org/10.1021/ja058777l.

[36] D. Zhao, D. Yuan, H.C. Zhou, The current status of hydrogen storage in metal-organic frameworks, Energy and Environmental Science. 1 (2008) 222–235. https://doi.org/10.1039/b808322n.

[37] M.P. Suh, H.J. Park, T.K. Prasad, D.W. Lim, Hydrogen storage in metal-organic frameworks, Chemical Reviews. 112 (2012) 782–835. https://doi.org/10.1021/cr200274s.

[38] W.C. Xu, K. Takahashi, Y. Matsuo, Y. Hattori, M. Kumagai, S. Ishiyama, K. Kaneko, S. Iijima, Investigation of hydrogen storage capacity of various carbon materials, International Journal of Hydrogen Energy. 32 (2007) 2504–2512. https://doi.org/10.1016/j.ijhydene.2006.11.012.

[39] W. Hu, J. Huang, P. Yu, M. Zheng, Y. Xiao, H. Dong, Y. Liang, H. Hu, Y. Liu, Hierarchically Porous Carbon Derived from Neolamarckia cadamba for Electrochemical Capacitance and Hydrogen Storage, ACS Sustainable Chemistry and Engineering. 7 (2019) 15385–15393. https://doi.org/10.1021/acssuschemeng.9b02734.

[40] S.S. Samantaray, S.R. Mangisetti, S. Ramaprabhu, Investigation of room temperature hydrogen storage in biomass derived activated carbon, Journal of Alloys and Compounds. 789 (2019) 800–804. https://doi.org/10.1016/j.jallcom.2019.03.110.

[41] T. Otowa, R. Tanibata, M. Itoh, Production and adsorption characteristics of MAXSORB: High-surface-area active carbon, Gas Separation and Purification. 7 (1993) 241–245. https://doi.org/10.1016/0950-4214(93)80024-Q.

[42] M. Hu, J. Reboul, S. Furukawa, N.L. Torad, Q. Ji, P. Srinivasu, K. Ariga, S. Kitagawa, Y. Yamauchi, Direct carbonization of Al-based porous coordination polymer for synthesis of nanoporous carbon, J Am Chem Soc. 134 (2012) 2864–2867. https://doi.org/10.1021/ja208940u.

[43] S.J. Yang, T. Kim, J.H. Im, Y.S. Kim, K. Lee, H. Jung, C.R. Park, MOF-derived hierarchically porous carbon with exceptional porosity and hydrogen storage capacity, Chemistry of Materials. 24 (2012) 464–470. https://doi.org/10.1021/cm202554j.

[44] US Department of Energy, Target Explanation Document: Onboard Hydrogen Storage for Light-Duty Fuel Cell Vehicles, (2017). https://www.energy.gov/sites/prod/files/2017/05/f34/fcto_targets_onboard_hydro_storage_explanation.pdf (accessed October 15, 2020).

[45] H. Farabi-Asl, K. Itaoka, A. Chapman, E. Kato, A. Kurosawa, Key factors for achieving emission reduction goals cognizant of CCS, International Journal of Greenhouse Gas Control. 99 (2020) 103097. https://doi.org/10.1016/j.ijggc.2020.103097.

[46] D. Jansen, M. Gazzani, G. Manzolini, E. Van Dijk, M. Carbo, Pre-combustion CO2 capture, International Journal of Greenhouse Gas Control. 40 (2015) 167–187. https://doi.org/10.1016/j.ijggc.2015.05.028.

[47] M. Gazzani, E. Macchi, G. Manzolini, CO2 capture in natural gas combined cycle with SEWGS. Part A: Thermodynamic performances, International Journal of Greenhouse Gas Control. 12 (2013) 493–501. https://doi.org/10.1016/j.ijggc.2012.06.010.

[48] C. Song, W. Pan, S.T. Srimat, J. Zheng, Y. Li, Y.H. Wang, B.Q. Xu, Q.M. Zhu, Tri-reforming of methane over Ni catalysts for CO2 conversion to Syngas with desired H2CO ratios using flue gas of power plants without CO2 separation, in: Studies in Surface Science and Catalysis, Elsevier Inc., 2004: pp. 315–322. https://doi.org/10.1016/s0167-2991(04)80270-2.

[49] M. Hasib-ur-Rahman, M. Siaj, F. Larachi, CO 2 capture in alkanolamine/room-temperature ionic liquid emulsions: A viable approach with carbamate crystallization and curbed corrosion behavior, International Journal of Greenhouse Gas Control. 6 (2012) 246–252. https://doi.org/10.1016/j.ijggc.2011.10.014.

[50] S. Liu, L. Rao, P. Yang, X. Wang, L. Wang, R. Ma, L. Yue, X. Hu, Superior CO2 uptake on nitrogen doped carbonaceous adsorbents from commercial phenolic resin, Journal of Environmental Sciences. 93 (2020) 109–116. https://doi.org/10.1016/J.JES.2020.04.006.

[51] C. Ma, T. Lu, J. Shao, J. Huang, X. Hu, L. Wang, Biomass derived nitrogen and sulfur co-doped porous carbons for efficient CO2 adsorption, Separation and Purification Technology. 281 (2022) 119899. https://doi.org/10.1016/J.SEPPUR.2021.119899.

[52] J. Shao, C. Ma, J. Zhao, L. Wang, X. Hu, Effective nitrogen and sulfur co-doped porous carbonaceous CO2 adsorbents derived from amino acid, Colloids and Surfaces A: Physicochemical and Engineering Aspects. 632 (2022) 127750. https://doi.org/10.1016/J.COLSURFA.2021.127750.

[53] F. Yang, J. Wang, L. Liu, P. Zhang, W. Yu, Q. Deng, Z. Zeng, S. Deng, Synthesis of Porous Carbons with High N-Content from Shrimp Shells for Efficient CO2-Capture and Gas Separation, ACS Sustainable Chemistry and Engineering. 6 (2018) 15550–15559. https://doi.org/10.1021/ACSSUSCHEMENG.8B03995/SUPPL_FILE/SC8B03995_SI_001.PDF.

[54] X. Ma, L. Li, R. Chen, C. Wang, H. Li, H. Li, Highly Nitrogen-Doped Porous Carbon Derived from Zeolitic Imidazolate Framework-8 for CO2 Capture, Chemistry – An Asian Journal. 13 (2018) 2069–2076. https://doi.org/10.1002/ASIA.201800548.

[55] J.H. Choe, H. Kim, C.S. Hong, MOF-74 type variants for CO2 capture, Materials Chemistry Frontiers. 5 (2021) 5172–5185. https://doi.org/10.1039/D1QM00205H.

[56] G. Avci, S. Velioglu, S. Keskin, High-Throughput Screening of MOF Adsorbents and Membranes for H2 Purification and CO2 Capture, ACS Applied Materials and Interfaces. 10 (2018) 33693–33706. https://doi.org/10.1021/ACSAMI.8B12746/ASSET/IMAGES/LARGE/AM-2018-12746P_0008.JPEG.

[57] S. Kumar, R. Srivastava, J. Koh, Utilization of zeolites as CO2 capturing agents: Advances and future perspectives, Journal of CO2 Utilization. 41 (2020) 101251. https://doi.org/10.1016/J.JCOU.2020.101251.

[58] J. Serafin, U. Narkiewicz, A.W. Morawski, R.J. Wróbel, B. Michalkiewicz, Highly microporous activated carbons from biomass for CO2 capture and effective micropores at different conditions, Journal of CO2 Utilization. 18 (2017) 73–79. https://doi.org/10.1016/j.jcou.2017.01.006.

[59] V. Presser, J. McDonough, S.H. Yeon, Y. Gogotsi, Effect of pore size on carbon dioxide sorption by carbide derived carbon, Energy and Environmental Science. 4 (2011) 3059–3066. https://doi.org/10.1039/c1ee01176f.

[60] L. Wang, R.T. Yang, Significantly increased CO 2 adsorption performance of nanostructured templated carbon by tuning surface area and nitrogen doping, Journal of Physical Chemistry C. 116 (2012) 1099–1106. https://doi.org/10.1021/jp2100446.

[61] K.V. Kumar, K. Preuss, L. Lu, Z.X. Guo, M.M. Titirici, Effect of Nitrogen Doping on the CO2 Adsorption Behavior in Nanoporous Carbon Structures: A Molecular Simulation Study, Journal of Physical Chemistry C. 119 (2015) 22310–22321. https://doi.org/10.1021/acs.jpcc.5b06017.

[62] W. Xing, C. Liu, Z. Zhou, L. Zhang, J. Zhou, S. Zhuo, Z. Yan, H. Gao, G. Wang, S.Z. Qiao, Superior CO2 uptake of N-doped activated carbon through hydrogen-bonding interaction, Energy and Environmental Science. 5 (2012) 7323–7327. https://doi.org/10.1039/c2ee21653a.

[63] D.H. Jeon, B.G. Min, J.G. Oh, C. Nah, S.J. Park, Influence of nitrogen moieties on CO2 capture of Carbon aerogel, Carbon Letters. 16 (2015) 57–61. https://doi.org/10.5714/CL.2015.16.1.057.

[64] X. Zhu, D.C.W. Tsang, L. Wang, Z. Su, D. Hou, L. Li, J. Shang, Machine learning exploration of the critical factors for CO2 adsorption capacity on porous carbon materials at different pressures, Journal of Cleaner Production. 273 (2020) 122915. https://doi.org/10.1016/j.jclepro.2020.122915.

[65] M. Choucair, P. Thordarson, J.A. Stride, Gram-scale production of graphene based on solvothermal synthesis and sonication, Nature Nanotechnology. 4 (2009) 30–33. https://doi.org/10.1038/nnano.2008.365.

[66] S.M. Lyth, Doped and Decorated Carbon Foams for Energy Applications, in: Nanocarbons for Energy Conversion: Supramolecular Approaches, 2019: pp. 175–203. https://doi.org/10.1007/978-3-319-92917-0_8.

[67] L. Speyer, S. Fontana, S. Cahen, C. Hérold, Simple production of high-quality graphene foams by pyrolysis of sodium ethoxide, Materials Chemistry and Physics. 219 (2018) 57–66. https://doi.org/10.1016/j.matchemphys.2018.08.020.

[68] J. Liu, D. Takeshi, K. Sasaki, S.M. Lyth, Defective Graphene Foam: A Platinum Catalyst Support for PEMFCs, Journal of The Electrochemical Society. 161 (2014) F838–F844. https://doi.org/10.1149/2.0231409jes.

[69] M. Choucair, P. Mauron, Versatile preparation of graphene-based nanocomposites and their hydrogen adsorption, International Journal of

Hydrogen Energy. 40 (2015) 6158–6164. https://doi.org/10.1016/j.ijhydene.2015.03.065.

[70] S.M. Lyth, Y. Nabae, N.M. Islam, T. Hayakawa, S. Kuroki, M.A. Kakimoto, S. Miyata, Solvothermal synthesis of nitrogen-containing graphene for electrochemical oxygen reduction in acid media, in: E-Journal of Surface Science and Nanotechnology, 2012: pp. 29–32. https://doi.org/10.1380/ejssnt.2012.29.

[71] A. Mufundirwa, G.F. Harrington, B. Smid, B. V. Cunning, K. Sasaki, S.M. Lyth, Durability of template-free Fe-N-C foams for electrochemical oxygen reduction in alkaline solution, Journal of Power Sources. 375 (2018) 244–254. https://doi.org/10.1016/j.jpowsour.2017.07.025.

[72] A. Mufundirwa, G.F. Harrington, M.S. Ismail, B. Šmid, B. V Cunning, Y. Shundo, M. Pourkashanian, K. Sasaki, A. Hayashi, S.M. Lyth, Gram-scale synthesis of alkoxide-derived nitrogen-doped carbon foam as a support for Fe–N–C electrocatalysts, Nanotechnology. 31 (2020) 225401. https://doi.org/10.1088/1361-6528/AB76ED.

[73] S.M. Lyth, J. Liu, A. Mufundirwa, B. Smid, S. Ma, P.J.A. Kenis, K. Sasaki, Gram-Scale Synthesis of Nitrogen-Doped Carbon Foams As Template-Free, Metal-Free, Non-Precious Electrocatalysts for Oxygen Reduction and CO2 Conversion, in: ECS Meeting Abstracts, 2016: p. 2770.

[74] D.P. Broom, Hydrogen storage materials : the characterisation of their storage properties, (2011) 258.

[75] P. Ramirez-Vidal, G. Sdanghi, A. Celzard, V. Fierro, High hydrogen release by cryo-adsorption and compression on porous materials, International Journal of Hydrogen Energy. 47 (2022) 8892–8915. https://doi.org/10.1016/J.IJHYDENE.2021.12.235.

[76] US National Institute of Standards and Technology, Thermophysical Properties of Fluid Systems, (2018). https://webbook.nist.gov/chemistry/fluid/ (accessed May 21, 2020).

[77] B. Panella, M. Hirscher, S. Roth, Hydrogen adsorption in different carbon nanostructures, Carbon N Y. 43 (2005) 2209–2214. https://doi.org/10.1016/J.CARBON.2005.03.037.

[78] X. Tang, N. Ripepi, S. Rigby, R. Mokaya, E. Gilliland, New perspectives on supercritical methane adsorption in shales and associated thermodynamics, Journal of Industrial and Engineering Chemistry. 78 (2019) 186–197. https://doi.org/10.1016/J.JIEC.2019.06.015.

[79] K. Srinivasan, B.B. Saha, K.C. Ng, P. Dutta, M. Prasad, A method for the calculation of the adsorbed phase volume and pseudo-saturation pressure from adsorption isotherm data on activated carbon, Physical Chemistry Chemical Physics. 13 (2011) 12559–12570. https://doi.org/10.1039/C1CP20383E.

[80] B. Carpenter, A. Gelman, M.D. Hoffman, D. Lee, B. Goodrich, M. Betancourt, M.A. Brubaker, J. Guo, P. Li, A. Riddell, Stan: A Probabilistic Programming Language, Journal of Statistical Software. 76 (2017) 1–32. https://doi.org/10.18637/JSS.V076.I01.

[81] J. Purewal, D. Liu, A. Sudik, M. Veenstra, J. Yang, S. Maurer, U. Müller, D.J. Siegel, Improved hydrogen storage and thermal conductivity in high-density MOF-5 composites, Journal of Physical Chemistry C. 116 (2012) 20199–20212. https://doi.org/10.1021/JP305524F/SUPPL_FILE/JP305524F_SI_001.PDF.

[82] M.A. Richard, P. Bénard, R. Chahine, Gas adsorption process in activated carbon over a wide temperature range above the critical point. Part 2: conservation of mass and energy, Adsorption 2009 15:1. 15 (2009) 53–63. https://doi.org/10.1007/S10450-009-9150-4.

[83] O. Talu, A.L. Myers, Rigorous thermodynamic treatment of gas adsorption, AIChE Journal. 34 (1988) 1887–1893. https://doi.org/10.1002/AIC.690341114.

[84] C.M. Simon, B. Smit, M. Haranczyk, PyIAST: Ideal adsorbed solution theory (IAST) Python package, Computer Physics Communications. 200 (2016) 364–380. https://doi.org/10.1016/j.cpc.2015.11.016.

[85] Y. Li, B. Zou, C. Hu, M. Cao, Nitrogen-doped porous carbon nanofiber webs for efficient CO2 capture and conversion, Carbon N Y. 99 (2016) 79–89. https://doi.org/10.1016/j.carbon.2015.11.074.

[86] J. Jagiello, C. Ania, J.B. Parra, C. Cook, Dual gas analysis of microporous carbons using 2D-NLDFT heterogeneous surface model and combined adsorption data of N2 and CO2, Carbon N Y. 91 (2015) 330–337. https://doi.org/10.1016/j.carbon.2015.05.004.

[87] T.S. Blankenship, N. Balahmar, R. Mokaya, Oxygen-rich microporous carbons with exceptional hydrogen storage capacity, Nature Communications. 8 (2017) 1–12. https://doi.org/10.1038/s41467-017-01633-x.

[88] Norah Balahmar, A. Salam Al-Jumialy, Robert Mokaya, Biomass to porous carbon in one step: directly activated biomass for high performance CO 2 storage, Journal of Materials Chemistry A. 5 (2017) 12330–12339. https://doi.org/10.1039/C7TA01722G.

[89] D. DeSantis, J.A. Mason, B.D. James, C. Houchins, J.R. Long, M. Veenstra, Techno-economic Analysis of Metal–Organic Frameworks for Hydrogen and Natural Gas Storage, Energy and Fuels. 31 (2017) 2024–2032. https://doi.org/10.1021/ACS.ENERGYFUELS.6B02510.

[90] I.M. Lima, A. McAloon, A.A. Boateng, Activated carbon from broiler litter: Process description and cost of production, Biomass and Bioenergy. 32 (2008) 568–572. https://doi.org/10.1016/J.BIOMBIOE.2007.11.008.

[91] N. Ferralis, Probing mechanical properties of graphene with Raman spectroscopy, Journal of Materials Science. 45 (2010) 5135–5149. https://doi.org/10.1007/s10853-010-4673-3.

[92] M.S. Dresselhaus, A. Jorio, A.G. Souza Filho, R. Saito, Defect characterization in graphene and carbon nanotubes using Raman spectroscopy, Trans. R. Soc. A. 368 (2010) 5355–5377. https://doi.org/10.1098/rsta.2010.0213.

[93] J. Cai, J. Qi, C. Yang, X. Zhao, Poly(vinylidene chloride)-based carbon with ultrahigh microporosity and outstanding performance for CH4 and H2 storage

and CO 2 capture, ACS Applied Materials and Interfaces. 6 (2014) 3703–3711. https://doi.org/10.1021/am500037b.

[94] T. Kim, J. Lee, K.H. Lee, Full graphitization of amorphous carbon by microwave heating, RSC Advances. 6 (2016) 24667–24674. https://doi.org/10.1039/c6ra01989g.

[95] I. Suárez-Ruiz, J.C. Crelling, Coal-Derived Carbon Materials, in: Applied Coal Petrology, Elsevier Ltd, 2008: pp. 193–225. https://doi.org/10.1016/B978-0-08-045051-3.00008-7.

[96] A.G. Shard, Detection limits in XPS for more than 6000 binary systems using Al and Mg Kα X-rays, Surface and Interface Analysis. 46 (2014) 175–185. https://doi.org/10.1002/SIA.5406.

[97] K. Artyushkova, Misconceptions in interpretation of nitrogen chemistry from x-ray photoelectron spectra, Journal of Vacuum Science & Technology A. 38 (2020) 031002. https://doi.org/10.1116/1.5135923.

[98] M. Thommes, K. Kaneko, A. V Neimark, J.P. Olivier, F. Rodriguez-Reinoso, J. Rouquerol, K.S.W. Sing, Physisorption of gases, with special reference to the evaluation of surface area and pore size distribution (IUPAC Technical Report), Pure and Applied Chemistry. 87 (2015) 1051–1069.

[99] M. Inagaki, M. Toyoda, Y. Soneda, T. Morishita, Nitrogen-doped carbon materials, Carbon N Y. 132 (2018) 104–140. https://doi.org/10.1016/j.carbon.2018.02.024.

[100] H. Li, J. Li, A. Thomas, Y. Liao, Ultra- High Surface Area Nitrogen- Doped Carbon Aerogels Derived From a Schiff- Base Porous Organic Polymer Aerogel for CO_2 Storage and Supercapacitors, Advanced Functional Materials. 29 (2019) 1904785. https://doi.org/10.1002/adfm.201904785.

[101] Z. Yong, V.G. Mata, A.E. Rodrigues, Adsorption of carbon dioxide on chemically modified high surface area carbon-based adsorbents at high temperature, Adsorption. 7 (2001) 41–50. https://doi.org/10.1023/A:1011220900415.

[102] J.H. Park, S.J. Park, Expansion of effective pore size on hydrogen physisorption of porous carbons at low temperatures with high pressures, Carbon N Y. 158 (2020) 364–371. https://doi.org/10.1016/J.CARBON.2019.10.100.

[103] M.I.M. Kusdhany, S.M. Lyth, New insights into hydrogen uptake on porous carbon materials via explainable machine learning, Carbon N Y. 179 (2021) 190–201. https://doi.org/10.1016/j.carbon.2021.04.036.

[104] G. Sethia, A. Sayari, Activated carbon with optimum pore size distribution for hydrogen storage, Carbon N Y. 99 (2016) 289–294. https://doi.org/10.1016/j.carbon.2015.12.032.

[105] Y. Xia, G.S. Walker, D.M. Grant, R. Mokaya, Hydrogen storage in high surface area carbons: Experimental demonstration of the effects of nitrogen doping, J Am Chem Soc. 131 (2009) 16493–16499. https://doi.org/10.1021/ja9054838.

[106] W. Zhao, V. Fierro, N. Fernández-Huerta, M.T. Izquierdo, A. Celzard, Hydrogen uptake of high surface area-activated carbons doped with nitrogen, International

Journal of Hydrogen Energy. 38 (2013) 10453–10460. https://doi.org/10.1016/j.ijhydene.2013.06.048.

[107] J. Rouquerol, F. Rouquerol, P. Llewellyn, G. Maurin, K. Sing, Adsorption by Powders and Porous Solids, 2nd Edition, 2012.

[108] N.P. Stadie, J.J. Vajo, R.W. Cumberland, A.A. Wilson, C.C. Ahn, B. Fultz, Zeolite-templated carbon materials for high-pressure hydrogen storage, Langmuir. 28 (2012) 10057–10063. https://doi.org/10.1021/la302050m.

[109] S.J. Yang, J.H. Im, H. Nishihara, H. Jung, K. Lee, T. Kyotani, C.R. Park, General relationship between hydrogen adsorption capacities at 77 and 298 K and pore characteristics of the porous adsorbents, Journal of Physical Chemistry C. 116 (2012) 10529–10540. https://doi.org/10.1021/jp302304w.

[110] Z. Chen, P. Li, R. Anderson, X. Wang, X. Zhang, L. Robison, L.R. Redfern, S. Moribe, T. Islamoglu, D.A. Gómez-Gualdrón, T. Yildirim, J.F. Stoddart, O.K. Farha, Balancing volumetric and gravimetric uptake in highly porous materials for clean energy, Science (1979). 368 (2020) 297–303. https://doi.org/10.1126/science.aaz8881.

[111] G. Sdanghi, S. Schaefer, G. Maranzana, A. Celzard, V. Fierro, Application of the modified Dubinin-Astakhov equation for a better understanding of high-pressure hydrogen adsorption on activated carbons, International Journal of Hydrogen Energy. 45 (2020) 25912–25926. https://doi.org/10.1016/J.IJHYDENE.2019.09.240.

[112] V.P. Ting, A.J. Ramirez-Cuesta, N. Bimbo, J.E. Sharpe, A. Noguera-Diaz, V. Presser, S. Rudic, T.J. Mays, Direct Evidence for Solid-like Hydrogen in a Nanoporous Carbon Hydrogen Storage Material at Supercritical Temperatures, ACS Nano. 9 (2015) 8249–8254. https://doi.org/10.1021/ACSNANO.5B02623/SUPPL_FILE/NN5B02623_SI_001.PDF.

[113] S.K. Bhatia, A.L. Myers, Optimum conditions for adsorptive storage, Langmuir. 22 (2006) 1688–1700. https://doi.org/10.1021/LA0523816/ASSET/IMAGES/MEDIUM/LA0523816N00001.GIF.

[114] M.L. Gray, K.J. Champagne, D. Fauth, J.P. Baltrus, H. Pennline, Performance of immobilized tertiary amine solid sorbents for the capture of carbon dioxide, International Journal of Greenhouse Gas Control. 2 (2008) 3–8. https://doi.org/10.1016/S1750-5836(07)00088-6.

[115] J.H. Lee, H.J. Lee, S.Y. Lim, B.G. Kim, J.W. Choi, Combined CO2-philicity and Ordered Mesoporosity for Highly Selective CO2 Capture at High Temperatures, J Am Chem Soc. 137 (2015) 7210–7216. https://doi.org/10.1021/JACS.5B03579.

[116] S. Wang, Z. Zhang, S. Dai, D. Jiang, Insights into CO 2 /N 2 Selectivity in Porous Carbons from Deep Learning, ACS Materials Letters. 1 (2019) 558–563. https://doi.org/10.1021/acsmaterialslett.9b00374.

[117] Neal. Fairley, A. Carrick, The Casa cookbook, 2005. http://www.casaxps.com (accessed January 21, 2022).

[118] L.Y. Molefe, N.M. Musyoka, J. Ren, H.W. Langmi, P.G. Ndungu, R. Dawson, M. Mathe, Synthesis of porous polymer-based metal–organic frameworks monolithic hybrid composite for hydrogen storage application, Journal of Materials Science. 54 (2019) 7078–7086. https://doi.org/10.1007/s10853-019-03367-1.

[119] S. Rochat, K. Polak-Kraśna, M. Tian, L.T. Holyfield, T.J. Mays, C.R. Bowen, A.D. Burrows, Hydrogen storage in polymer-based processable microporous composites, Journal of Materials Chemistry A. 5 (2017) 18752–18761. https://doi.org/10.1039/c7ta05232d.

[120] Y.W. You, E.H. Moon, I. Heo, H. Park, J.S. Hong, J.K. Suh, Preparation and characterization of porous carbons from ion-exchange resins with different degree of cross-linking for hydrogen storage, Journal of Industrial and Engineering Chemistry. 45 (2017) 164–170. https://doi.org/10.1016/j.jiec.2016.09.019.

[121] A. Ahmed, S. Seth, J. Purewal, A.G. Wong-Foy, M. Veenstra, A.J. Matzger, D.J. Siegel, Exceptional hydrogen storage achieved by screening nearly half a million metal-organic frameworks, Nature Communications. 10 (2019) 1–9. https://doi.org/10.1038/s41467-019-09365-w.

[122] K.S. Lin, A.K. Adhikari, C.N. Ku, C.L. Chiang, H. Kuo, Synthesis and characterization of porous HKUST-1 metal organic frameworks for hydrogen storage, International Journal of Hydrogen Energy. 37 (2012) 13865–13871. https://doi.org/10.1016/j.ijhydene.2012.04.105.

[123] S.J. Park, S.Y. Lee, A study on hydrogen-storage behaviors of nickel-loaded mesoporous MCM-41, Journal of Colloid and Interface Science. 346 (2010) 194–198. https://doi.org/10.1016/j.jcis.2010.02.047.

[124] S.N. Klyamkin, S. V. Chuvikov, N. V. Maletskaya, E. V. Kogan, V.P. Fedin, K.A. Kovalenko, D.N. Dybtsev, High-pressure hydrogen storage on modified MIL-101 metal-organic framework, International Journal of Energy Research. 38 (2014) 1562–1570. https://doi.org/10.1002/er.3175.

[125] J.A. Villajos, G. Orcajo, G. Calleja, J.A. Botas, C. Martos, Beneficial cooperative effect between Pd nanoparticles and ZIF-8 material for hydrogen storage, International Journal of Hydrogen Energy. 41 (2016) 19439–19446. https://doi.org/10.1016/j.ijhydene.2016.05.143.

[126] Y. Li, R.T. Yang, Hydrogen storage in metal-organic and covalent-organic frameworks by spillover, AIChE Journal. 54 (2008) 269–279. https://doi.org/10.1002/aic.11362.

[127] H. Yuan, J. Chen, D. Li, H. Chen, Y. Chen, 5 Ultramicropore-rich renewable porous carbon from biomass tar with excellent adsorption capacity and selectivity for CO2 capture, Chemical Engineering Journal. 373 (2019) 171–178. https://doi.org/10.1016/j.cej.2019.04.206.

[128] M. Liu, L. Shao, J. Huang, Y.N. Liu, O-containing hyper-cross-linked polymers and porous carbons for CO2 capture, Microporous and Mesoporous Materials. 264 (2018) 104–111. https://doi.org/10.1016/j.micromeso.2017.12.036.

[129] L. Hong, S. Ju, X. Liu, Q. Zhuang, G. Zhan, X. Yu, Highly Selective CO2 Uptake in Novel Fishnet-like Polybenzoxazine-Based Porous Carbon, Energy and Fuels. 33 (2019) 11454–11464. https://doi.org/10.1021/acs.energyfuels.9b02631.

Tables

Table 1. Synthesis yield after different stages of the synthesis procedure for carbon foam (CF) and nitrogen-doped carbon foam (NCF).

Sample	Yield after Mixing (wt%)	Mass After Mixing (g)	Yield After Pyrolysis (wt%)	Mass After Pyrolysis (g)	Product Yield (wt%)*	Product Mass (g)
CF	N/A	N/A	65	13.0	4.2 (10.1)	0.85
NCF	86	20.6	47	11.3	5.6 (12)	1.34

**Values in parenthesis correspond to the yield of elemental carbon in the final product compared to the precursors.*

Table 2. Atomic concentration of elements from XPS analysis. The standard error is calculated using a Monte Carlo method available within the software CasaXPS.[117]

	Relative Abundance (at%)			
Sample	C	N	O	Na
CF	93.4±2.3	1.1±2.3	4.4±0.9	1.1±0.4
NCF	87.6±1.6	7.0±1.5	5.2±0.7	0.2±0.3
MSC-30	97.1±2.0	0.4±1.8	2.5±0.8	N/A

Table 3. Textural properties of the different carbon samples.

Sample	S_{Mic}[a] (m^2/g)	S_{BET}[b] (m^2/g)	S_{Mic}/S_{BET}	V_{MP}[c] (cm^3/g)	V_{UM}[d] (cm^3/g)	V_{Mic}[e] (cm^3/g)	V_T[f] (cm^3/g)	V_{Mic}/V_T	$2t$[g] (nm)
CF	3156	3452	0.93	1.64	0.26	1.14 (1.61)	2.19	0.74	1.01
NCF	2704	2646	1.03	1.22	0.28	0.98 (1.17)	1.25	0.94	0.86
MSC-30	3166	3354	0.95	1.77	0.13	1.04 (1.68)	1.82	0.92	1.06

a. Micropore surface area determined using de Boer's t-plot method; b. Total surface area determined using BET method with Rouquerol's criteria used to select fitting pressure range (Figure S7); c. Micropore volume determined using the MP method; d. Ultramicropore volume from NLDFT using dual gas analysis (CO_2/N_2); e. Micropore volume from NLDFT (in brackets: micropore volume from t-plot, with fits shown in Figure S8); f. Total pore volume from the amount of cryogenic N_2 uptake at $P/P_0=0.99$; g. Peak micropore diameter from t-plot.

Table 4. Comparison of hydrogen uptake at 77K for various porous adsorbents reported in the literature.

Sample	S_{BET} (m^2/g)	Excess uptake at 0.1 MPa (wt%)	Total uptake at high pressure (wt%)	Reference
CF	3452	2.69	11.0 (9.5 MPa)	This study
NCF	2646	2.73	8.1 (9.5 MPa)	This study
MSC-30	3354	2.76	10.3 (9.5 MPa)	This study
PIM-1/MIL-101 (Cr)	2347	1.73	-	[118]
PAF-1	3787	1.43	9.18 (10 MPa)	[119]
KOH-activated olive stones	1173	2	2.96 (2.5 MPa)	[19]
Ion-exchange resin derived carbon	2561	2.5	3.5 (1 MPa)	[120]
MOF-5	3512	-	8 (10 MPa)	[121]
IRMOF-20	4073	-	10 (10 MPa)	[121]
MCM-41	1060	0.51	2.01 (3.5 MPa)	[28]
HKUST-1	1009	1.95	-	[122]
Used Cigarette Filter (SF-4600)	4310	4.0	11.2 (4.0 MPa)	[25]

Table 5. Comparison of hydrogen uptake at 298K with other porous materials reported in the literature.

Sample	S_{BET} (m^2/g)	Excess uptake (wt%)	Total uptake (wt%)	Reference
CF	3452	0.94 (9.5 MPa)	2.50 (9.5 MPa)	This study
NCF	2646	0.95 (9.5 MPa)	1.87 (9.5 MPa)	This study
MSC-30	3354	0.72 (9.5 MPa)	2.04 (9.5 MPa)	This study
MSC-30	3244	0.79 (10 MPa)	-	[108]
MSC-30 [303K]	3306	0.67 (10 MPa)	-	[38]
Ni-doped MCM-41	1214	0.68 (9.5 MPa)	-	[123]
NU-1501-Al	7310	0.8 (10 MPa)	2.9 (10 MPa)	[110]
NU-1500-Al	3560	-	2 (10 MPa)	[110]
Pt/C and MIL-101 Composite	1780	1.5 (100 MPa)	6.1 (100 MPa)	[124]
Ion-exchange resin derived carbon	2539	0.8 (20 MPa)	-	[120]
Pd/ZIF-8	1709	0.35 (10 MPa)	-	[125]
HKUST-1	1296	0.35 (10 MPa)	-	[126]
MIL-101	2931	0.51 (10 MPa)	-	[126]
COF-1	628	0.26 (10 MPa)	-	[126]

Table 6. Selectivity of the samples under different conditions.

Sample	CO_2/N_2 at 273K		CO_2/N_2 at 298K		CO_2/H_2 at 298K
	IAST[a]	Henry's Law	IAST[a]	Henry's Law	IAST[b]
CF	10	9	9	9	63
NCF	14	11	10	9	63
MSC-30	8	7	7	6	56

a. Values taken at 100 kPa; b. Values taken at 500 kPa.

Table 7. Comparison of CO_2 uptake and selectivity between the porous carbons measured in this study and those reported in the literature.

Sample Name	V_{Meso} (cm^3/g)	V_{Mic} (cm^3/g)	V_{UM} (cm^3/g)	BET SSA (m^2/g)	CO_2 uptake at 273K and 100 kPa (mmol/g)	CO_2 uptake at 298K and 100 kPa (mmol/g)	CO_2/N_2 selectivity at 273K	Reference
CF	0.55	1.61	0.26	3452	5.65	3.37	9	This study
NCF	0.03	1.17	0.28	2646	5.79	3.26	11	This study
MSC-30	0.05	1.68	0.13	3354	4.57	2.49	7	This study
PC-1-3	0.862	0.513	0.039	2424	4.1	2.66	9.6	[127]
PC-2-3	1.361	0.485	0.381	1829	5.03	3.13	15.4	[127]
NET2-1-700-2	0.11	0.64	0.27	1411	6.3	3.7	22.5	[128]
NET2-2-700-2	0.21	0.90	0.20	2091	5.2	2.9	19.9	[128]
PBZC-3-700	0.01	0.64	0.58	1065	7.10	4.43	34	[129]
PBZC-3-800	0.08	0.78	0.63	1414	8.44	4.98	37	[129]

Figures

Figure 1. SEM images of CF (a, b), NCF (c, d), and MSC-30 (e, f) at two different magnifications.

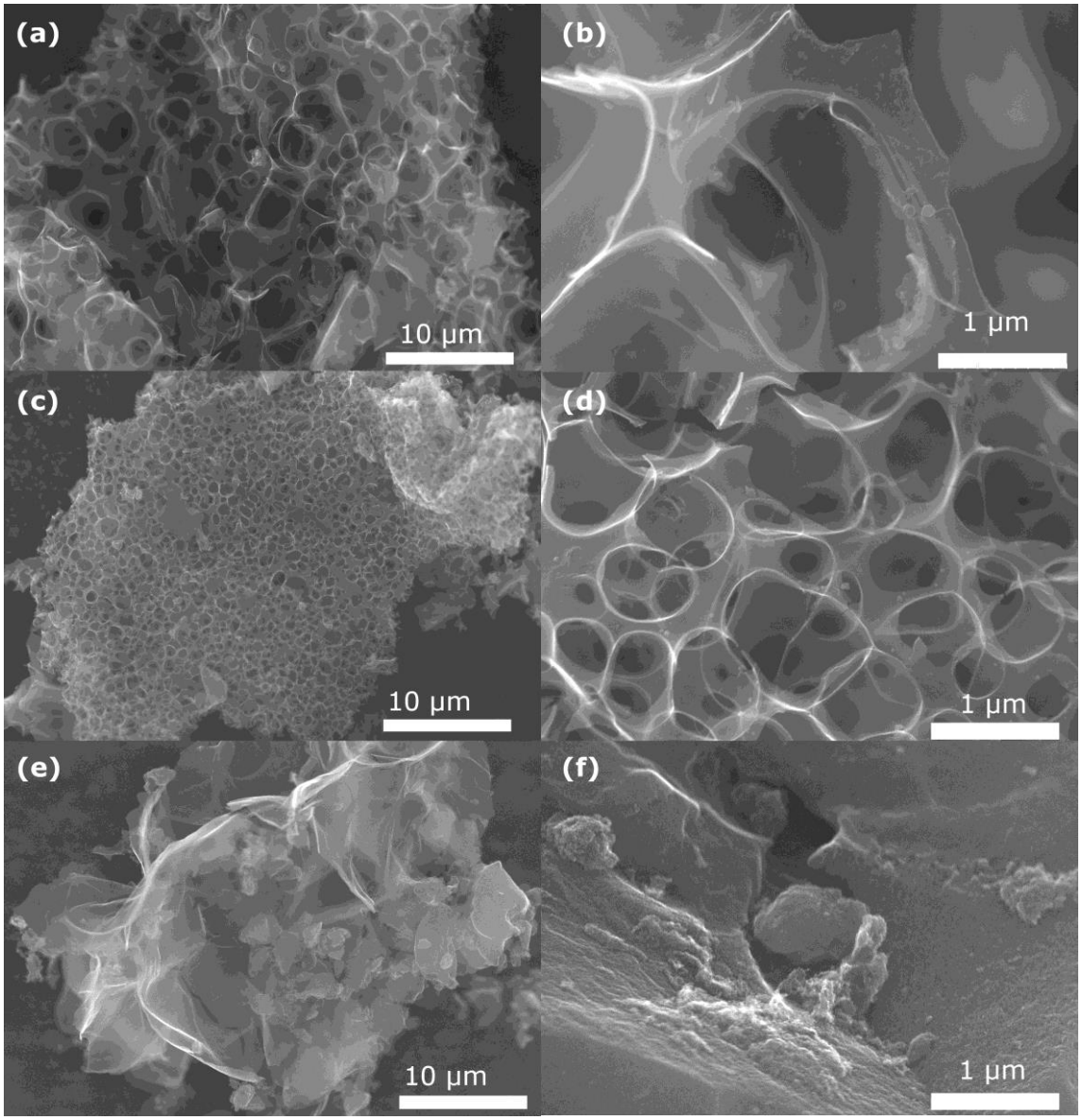

Figure 2. NCF XPS N1s spectrum with deconvolution.

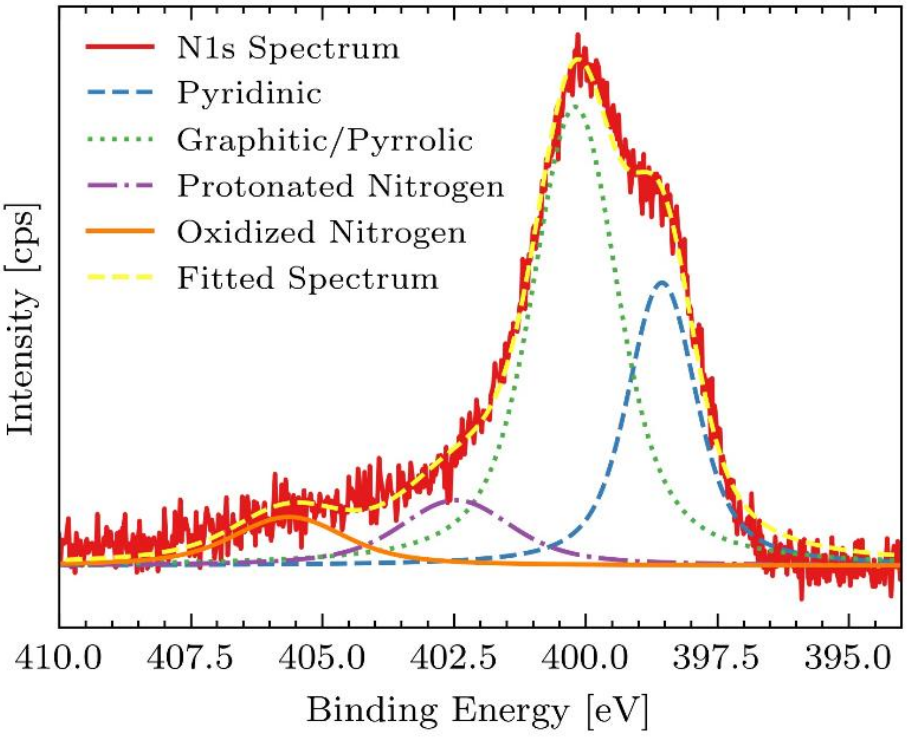

Figure 3. (a) N_2 adsorption-desorption isotherms at 77K, (b) pore size distribution from NLDFT, (c) cumulative pore volume from NLDFT.

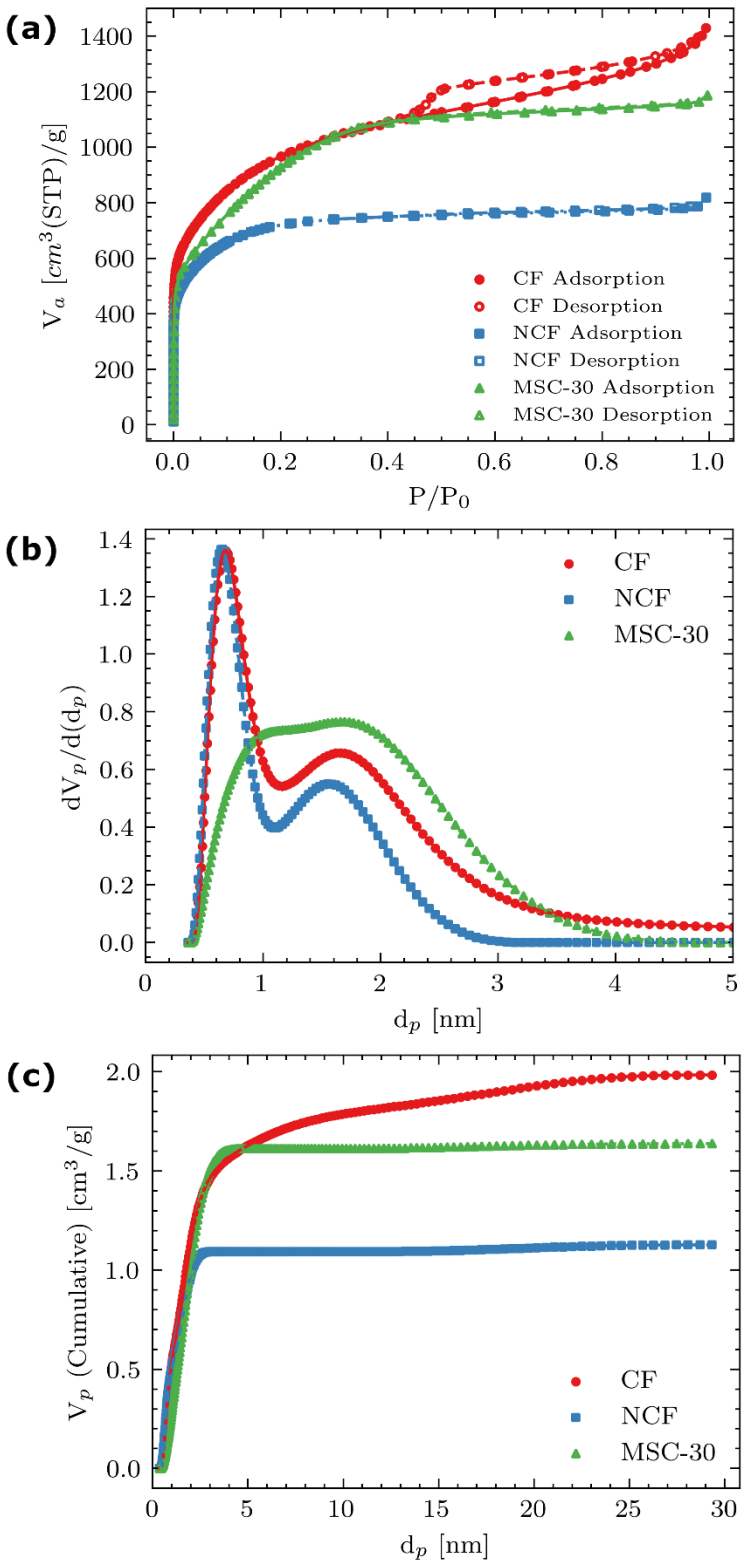

Figure 4. Hydrogen uptake at 77 K: (a) excess hydrogen uptake (measured); (b) total hydrogen uptake (calculated from Eq. 1); (c) excess hydrogen uptake normalized to surface area; and (d) excess hydrogen uptake normalized to the micropore surface area.

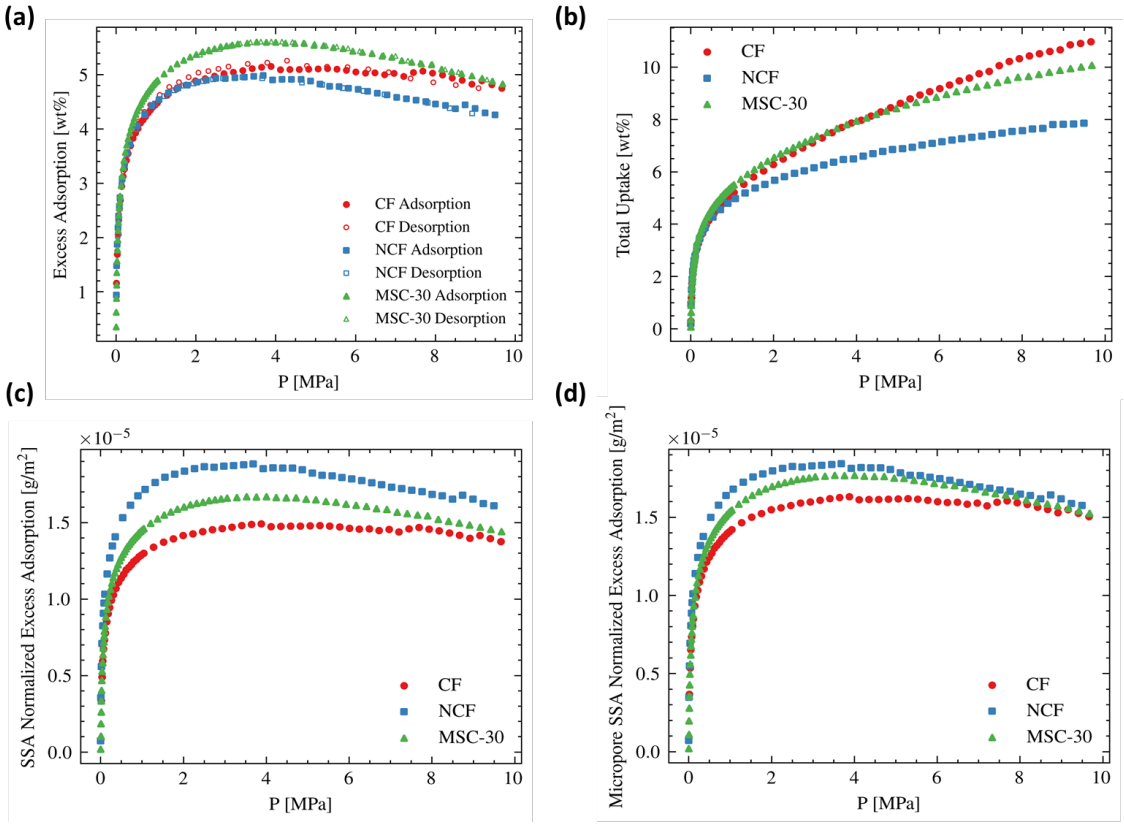

Figure 5. Hydrogen uptake at 298 K: (a) excess hydrogen uptake (measured); (b) total hydrogen uptake (calculated from Equation 1); (c) excess hydrogen uptake normalized to surface area.

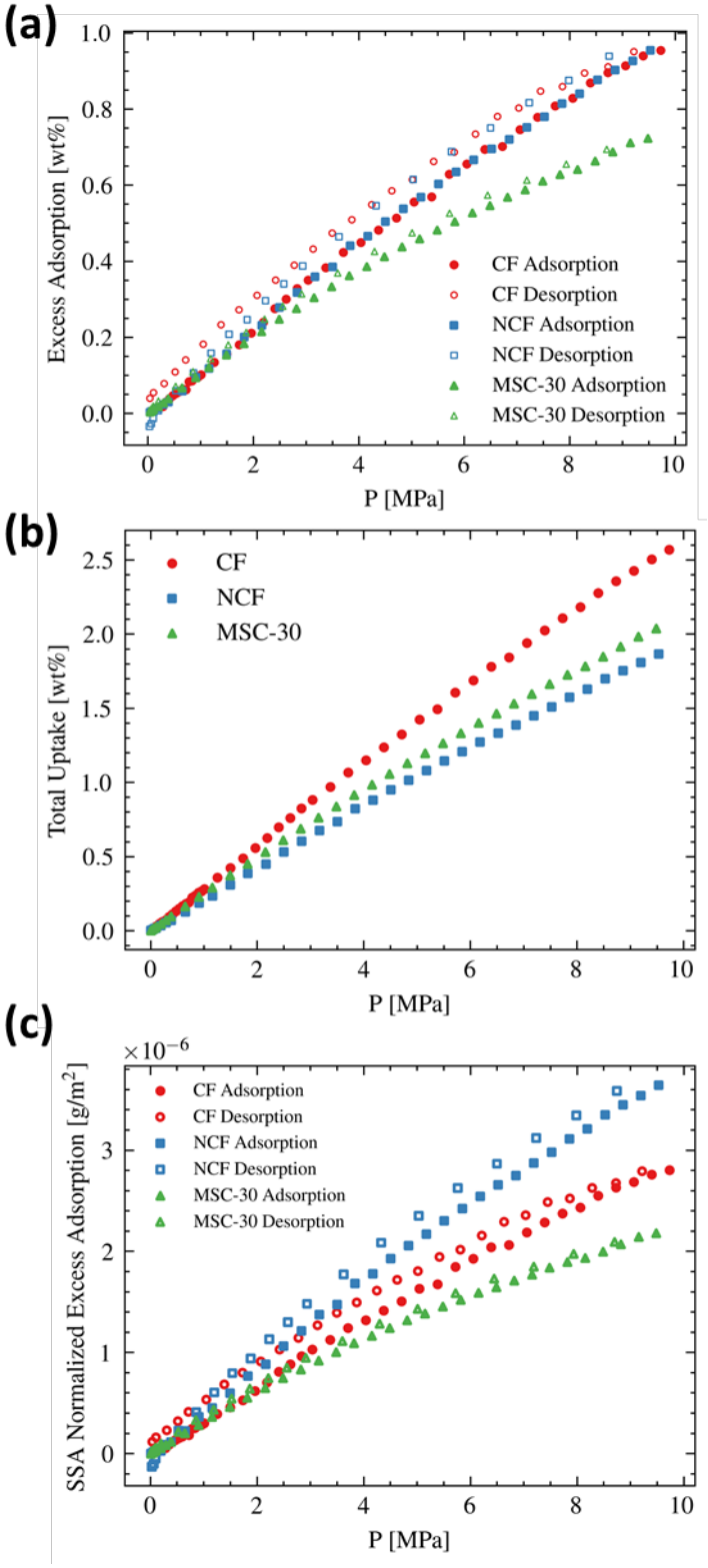

Figure 6. Variation in the heat of adsorption with absolute adsorption and temperature. The heat of adsorption for MSC-30 is calculated using the Unilan equation, which is temperature-dependent. Meanwhile, the heats of adsorption for CF and NCF are calculated from the MDA equation, which is independent of temperature. The dashed lines indicate 95% credible intervals calculated from the model parameters.

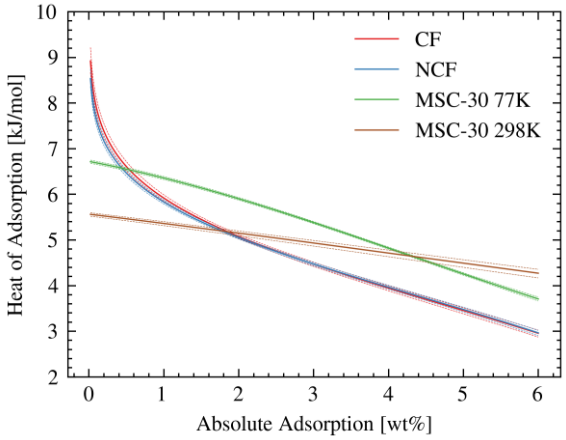

Figure 7. (a) CO_2 adsorption (filled symbols) and desorption (unfilled symbols) data up to 0.5 MPa and (b) normalized to surface area.

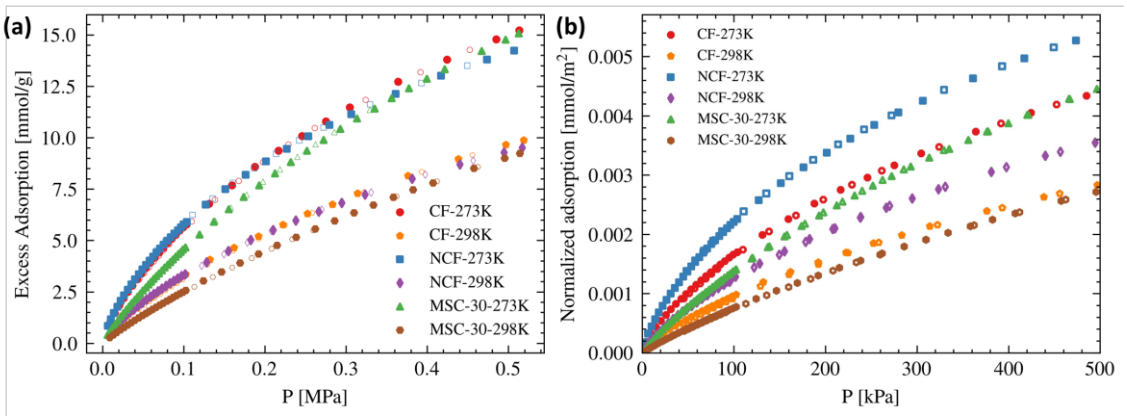

Figure 8. Heat of adsorption of the different carbon materials at various CO_2 loadings at (a) 273 K and (b) 298 K. The dashed lines indicate the 95% credible intervals from uncertainties in the MDA model parameters.

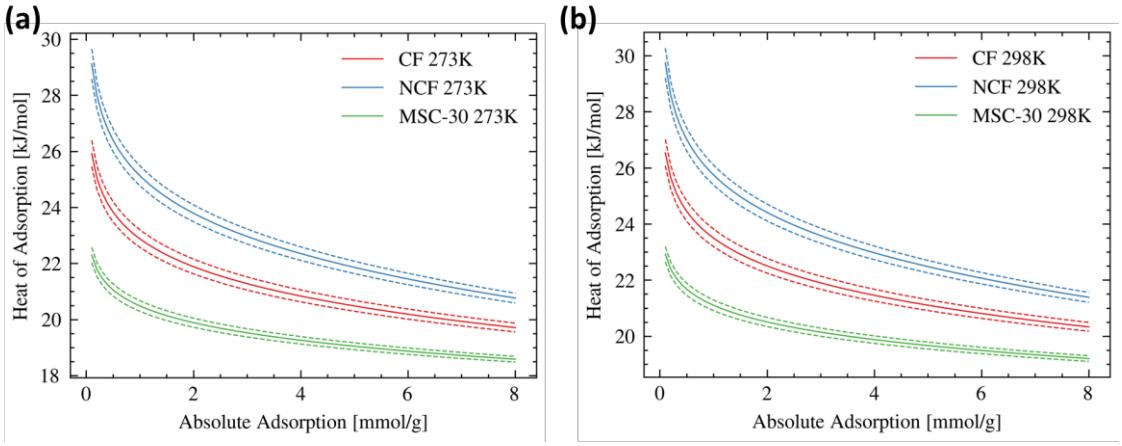

Figure 9. Bar charts comparing the adsorption performance of different samples.